Conformation-dependent influences of hydrophobic amino acids in two in-register parallel β-sheet amyloids, an α-synuclein amyloid and a local structural model of PrP^{Sc}

Hiroki Otaki[1†], Yuzuru Taguchi[2†]*, and Noriyuki Nishida[2]

1 Center for Bioinformatics and Molecular Medicine, Nagasaki University Graduate School of Biomedical Sciences, Nagasaki, Japan; otaki@nagasaki-u.ac.jp

2 Division of Cellular and Molecular Biology, Nagasaki University Graduate School of Biomedical Sciences, Nagasaki, Japan; noribaci@nagasaki-u.ac.jp

[†]The two authors equally contributed to the work.

* To whom correspondence should be addressed: ytaguchi@nagasaki-u.ac.jp

Abstract

Prions are pathogens which consist solely of abnormal isoform of prion protein (PrP^{Sc}) without any genetic material, and they therefore depend on purely protein-based mechanism for diversification and maintenance of pathogenic properties/information for strain diversity that has not been fully elucidated. According to the protein-only hypothesis, pathogenic properties of prions are determined by conformations of the constituent PrP^{Sc}, and alterations to even a single residue can drastically change the properties when the residue is located at a critical position for the structure of PrP^{Sc}. Interestingly, differences between polymorphic or species-specific residues that are responsible for species/strain barriers of prions are often caused by conservative replacements between hydrophobic amino acids. This implies that subtle differences among hydrophobic amino acids are significant for structures of PrP^{Sc}, and each hydrophobic amino acid have unique effects. Specifically how they are unique is difficult to demonstrate due to lack of detailed structures of PrP^{Sc}. Here we analyzed influences of different hydrophobic residues on structures of an in-register parallel β-sheet amyloid of α-synuclein (αSyn) by molecular dynamics (MD) simulation, and applied the knowledge from the αSyn amyloid to design local structures of human PrP^{Sc}, encompassing residues 107-143. On the local structural model, we assessed influences of polymorphisms known to affect clinical phenotypes of prion diseases. MD simulations of the αSyn amyloid revealed that methionine uniquely stabilized a U-shaped β-arch of the αSyn amyloid, whereas other hydrophobic amino acids destabilized it. The stabilizing effect of methionine was attributable to the long side chain without Cβ branching. The local structural model of PrP^{Sc} also revealed unique effects of hydrophobic amino acids depending on regional structures. Our study demonstrated specifically how and in what structure of in-register parallel β-sheet amyloids hydrophobic residues can exert unique effects and provide insights into the molecular mechanism of strain diversity of prions and other pathogenic amyloids.

Introduction

Prion diseases are a group of neurodegenerative disorders which are characterized by accumulation of the abnormal isoform (PrP^{Sc}) of prion protein (PrP) in the central nervous system [1]. Prion diseases have three etiologies, i.e., sporadic, inherited and acquired, depending on how the causative PrP^{Sc} starts propagation in the body; in sporadic and inherited prion diseases, e.g., sporadic Creutzfeldt-Jakob disease (CJD) and fatal familial insomnia (FFI), respectively, the causative PrP^{Sc} are generated by spontaneous conformational conversion of endogenous normal isoform PrP (PrP^{C}) into PrP^{Sc} with or without aid by pathogenic mutations in PRNP gene. Acquired prion diseases are caused by intake of exogenous PrP^{Sc} as infectious agents, prions, e.g., epidemic bovine spongiform encephalopathy (BSE) in cattle [2] and chronic wasting disease (CWD) in cervids [3]. Prions behave similarly as viruses, with high infectivity, existence of many strains, species/strain barriers, and adaptation to new hosts, despite the lack of conventional genetic material. These virus-like pathogenic properties of prions are hypothesized to be enciphered in the conformations of PrP^{Sc}, i.e., protein-only hypothesis [1][4].

Indeed, pathogenic properties of prions and the consequent clinical phenotypes are greatly affected by the primary structure of constituent PrP^{Sc} even by alteration of a single residue, in accordance with the fundamental fact that conformations of proteins are determined by the primary structures. For example, in sporadic CJD, PrP deposition patterns, lesion profiles in the brain, clinical presentations, and apparent molecular sizes of protease-resistant cores of PrP^{Sc} are varied depending on whether the polymorphic codon 129 is methionine (Met; M129) or valine (Val; V129) [5]. A pathogenic mutation D178N of human PrP causes either FFI or familial CJD in association with M129 or V129, respectively [6]. The codon 129 polymorphism also determines susceptibility to prion infections, i.e., species/strain barriers: a vast majority of new-variant CJD cases which resulted from trans-species transmission of BSE to humans are homozygous for M129 [7][8]; the polymorphic codon 132 of elk PrP, either Met or leucine (Leu), which is equivalent to the codon 129 polymorphism of human PrP, also affects susceptibility to CWD [9][10]. From the viewpoint of the protein-only hypothesis, the polymorphisms should effect through structural alterations of the constituent PrP^{Sc}; however, specifically how the subtle differences between those hydrophobic amino acids affect structures of the PrP^{Sc} has not been identified yet. Detailed structures of PrP^{Sc} are necessary for the investigation but, with all currently available data, even whether PrP^{Sc} is an in-register parallel β-sheet amyloid or a β-solenoid is still controversial due to its incompatibility with conventional high-resolution structural analyses [11][12][13][14][15][16].

Not only by the Met/Val polymorphic codon 129, strain/species barriers of prions can be caused by conservative replacements between different groups of hydrophobic amino acids. In experiments with C-terminally-truncated Y145Stop mutant of human PrP and the counterparts of mouse and Syrian hamster PrPs, whether residue 138 or 139 (in human numbering throughout unless otherwise noted) is isoleucine (Ile) or Met was critical for efficient amyloid formation and cross-seeding among them [17][18]. In transmission of prions of sporadic CJD homozygous for M129 to transgenic mice expressing human-mouse chimeric PrP, I138M substitution substantially extended incubation periods [19]. M109 and M112 are influential on transmission efficiencies among different hamster species [20][21]. In an experiment observing influences of systematically-introduced mutations of mouse PrP on conversion efficiencies in scrapie-infected Neuro2a cells, Met at some positions, e.g., M213, were replaceable with other hydrophobic residues like Leu, whereas unreplaceable at other residues, e.g., M206 [22]. In

in-vitro cross-seeding between ovine PrP and cervine CWD, I208M (in ovine numbering) mutation showed profound influences on seeding efficiencies [23]. Given those documented facts, we were interested in effects of different hydrophobic residues on structures of in-register parallel β-sheet amyloids, particularly whether Met has unique properties than other hydrophobic amino acids, and started the investigation with an in-register parallel β-sheet amyloid of α-synuclein (αSyn) as a surrogate structural model for PrP^{Sc}, as we previously did [24][25].

αSyn amyloid is the main component of Lewy bodies, which is a hallmark of Parkinson's disease (PD) and dementia with Lewy bodies (DLB), and reportedly has prion-like properties including transmissibility and strain diversity [26]. For instance, αSyn forms various types of amyloids in vitro which are different in appearances, proteolytic fragment patterns, and cytotoxicity [27]. Moreover, αSyn amyloids isolated from DLB and multiple system atrophy have different proteolytic fragment patterns, suggestive of distinct conformations [28]. Those are highly reminiscent of prions and imply that prion-like properties are inherent in in-register parallel β-sheet structures. As detailed structures of αSyn amyloids have been determined by solid-state NMR (ssNMR) [29] or cryo-electron microscopy [30][31], we used a Greek-key αSyn amyloid (PDB ID: 2n0a [29]) to investigate effects of different hydrophobic residues on the in-register parallel β-sheet structures. The studies revealed that lengths and Cβ-branching of the side chains of hydrophobic residues are important for stability of local structures of the amyloid, particularly in a U-shaped β-arch. Then, we applied the knowledge from the αSyn amyloid to model a local structure of PrP^{Sc} encompassing residues 107 to 143 of human PrP, PrP(107-143), assuming that PrP^{Sc} is also an in-register parallel β-sheet amyloid. We assessed how mutations and polymorphisms associated with strain diversity of prions affect structures of the model amyloid.

Our studies demonstrated specifically how different types of hydrophobic amino acids affect structures of in-register parallel β-sheet amyloids of αSyn and PrP(107-143). We also found that structural stability of U-shaped β-arches require hydrophobic cores with well-balanced interactions among the constituent hydrophobic residues. Those knowledge from the present studies would advance our understanding about strain diversity of amyloids, and also aid in designing more plausible PrP^{Sc} models and other amyloids in the future.

Results and Discussion

Investigation of the mechanism of how G84M mutation stabilizes the αSyn amyloid

Predicted intrinsic propensities of αSyn(E61M) and αSyn(G84M)

To compare influences of hydrophobic amino acids on the local structures of αSyn amyloids, we introduced Met substitution at residues 61 (E61M) and 84 (G84M), where we previously investigated influences of Ile substitutions [24]. We first estimated alteration to intrinsic propensities of the mutant αSyn by secondary structure prediction algorithm [24][32][33]. They both raised local (Pα-Pc) values, and the positive-(Pα-Pc) areas coalesced across the loop regions (**Fig 1A, red circles, and 1B**). Notably, in the mutant αSyn with G84M, αSyn(G84M), the positive-value areas of (Pβ-Pα) and (Pβ-Pc) in residues 88-90 disappeared, making the C-terminal region solely (Pα-Pc)-positive. Those alterations in predicted propensity profiles by the mutations were consistent with high α-helix propensity of Met [34][35].

MD simulation of αSyn(E61M) and αSyn(G84M)

MD simulations of homo-oligomer amyloids of αSyn(E61M) and αSyn(G84M) revealed that both the mutations

tended to stabilize the local structures particularly when they induced new β-sheets in the nearby loops encompassing residues 57 to 62, loop(57-62), or residues 84 to 87, loop(84-87), respectively (**Fig 1C, insets**). The induction of β-sheets in loop(57-62) were mainly in chains C-H (**Fig 1C, left inset, and Fig 1D, red box**), unlike E61I-induced β-sheet which were mainly on the chain-A side [24]. Effects of G84M substitution were more impressive. The almost entire region C-terminal to residue 80, even including loop(84-87) converted to stable β-sheets (**Fig 1C, right inset, and Fig 1D, red and blue boxes of G84M**), in contrast to those of G84I substitution [24]. Unexpectedly, in the amyloid of αSyn(G84L) that showed a similar predicted propensity profiles as αSyn(G84M) with positive (Pα-Pc) values across loop(84-87) (**Fig 2A**), the loop region was substantially destabilized like that of αSyn(G84I) [24] (**Fig 2B, red circle, and 2C, red and blue boxes**). Being interested in the opposite effects of G84M and G84L despite their similar nature, we focused on the residue 84 and performed further in silico analyses to identify the underlying mechanisms.

Further analyses of αSyn with substitution at residue 84

The final status of 400 ns simulations were rather different between αSyn(G84M) and αSyn(G84L) amyloids; all the side chains of Met at residue 84 (M84) pointed inward of loop(84-87), whereas some side chains of Leu at residue 84 (L84) flipped and pointed outward (**Fig 2D**). Hydrophobic contact diagrams of the αSyn(G84M) and αSyn(G84L) amyloids clearly exhibited differences: M84 of αSyn(G84M) amyloid had intra-chain interactions evenly with residues 82 and 89 of the same chain in all the layers, and the interactions were rather reproducible (**Fig 2E, G84M, Run 1-3**). On the other hand, αSyn(G84L) amyloids only infrequently showed that pattern (**Fig 2E, G84L Run 1-3**), or rather similar to those of another destabilizing mutation G84I (**Fig 2E, G84I**) [24].

The difference between Met and other hydrophobic amino acids occurred as early as immediately after modeling by SCWRL4, where the side chains of L84 and I84 were set at the periphery of β-arches, as if being ready to flip (**Fig 3A, Before**). In contrast, M84 wedged deeply into the β-arches throughout the step (**Fig 3A, G84M**). To make the initial status same, we created another set of αSyn(G84L) and αSyn(G84I) amyloid models by replacing M84 residues of an energy-minimized αSyn(G84M) amyloid (**Fig 3A, "After" of G84M**) with Leu or Ile (**Supplementary Fig S1B**). After remodeling by SCWRL4, the side chains of chains F-J kept the same positions as those of αSyn(G84M) (**Fig 3B, blue circle**), although those of chains A-E were similar to those of the old models (**Fig 3B, red circle**). In MD simulation, differences between αSyn(G84M), αSyn(G84I) and αSyn(G84L) amyloids were more accentuated only in 5 ns: their hydrophobic contact diagrams (**Fig 3C**) were similar to those of 400 ns-runs, i.e., M84 constantly interacting with residues 82 and 89 while others showing unstable interactions, and the final status of side chains greatly differed (**Fig 3D**). Even relatively-stable one in a 5 ns-run substantially disordered in the extended run up to 100 ns, with some side chains flipped (**Fig 3E**). A mutant with valine, another hydrophobic amino acid with relatively short side chain with Cβ branching, αSyn(G84V), also showed similar hydrophobic contact diagrams (**Fig 3C, G84V**). Importantly, those results also proved that short MD simulations are enough for assessment of influences of mutations on in-register parallel β-sheet amyloids.

The unique stabilizing effects of M84 would be attributable to the long side chain which can extend across the β-arch like a "crossbeam". During the simulation, the ends of the side chains were fixed in the proximity of A89 (**Supplementary Movie (G84M)**). The intimate interactions with A89 reinforce the hydrophobic core and stabilize the β-arch. Possibly, Leu could not replace Met despite their similarity in hydrophobicity and non-branching Cβ, because its side chain is not long enough for stable interactions with A89. Even in reality, the subtle difference

between Met and Leu is significant in certain cases of prion propagation, as the Met/Leu polymorphism of elk PrP affects susceptibility to CWD infection [9][10]. The local structures of CWD-PrP^{Sc} around the polymorphic residue might be similar to the U-shaped loop of αSyn in terms that the long side chain of Met is essential for stability.

Modeling a local structure of PrP^{Sc} based on the knowledge from the αSyn amyloids

Given the knowledge from studies on αSyn amyloids [24][25], we attempted to model a local structure of PrP^{Sc} with a U-shaped loop. A region comprising a glycine (Gly)-rich motif encompassing 123-127 of human PrP was suitable for a U-shaped loop and, in addition, the anti-prion effect of valine at residue 127 (V127) against various sporadic CJD [36] which is reminiscent of the destabilizing effects of V84 in αSyn amyloid supported the presence of a U-shaped loop in the region. Moreover, structures of amyloid cores of Y145Stop-mutant PrP investigated with ssNMR was available although not in atomic resolution [16][37]. As amyloids of the Y145Stop-mutant induced infectious PrP^{Sc} and caused bona fide prion disease when inoculated in mice [38], the amyloid could share the similar local structures with full-length PrP^{Sc}. We therefore tentatively modeled local structures of PrP^{Sc} in a region 107-143, PrP(107-143), utilizing the structural model of the Y145Stop mutant propounded by Theint et al. [37] and the knowledge from the αSyn amyloid for stable β-arches, i.e., hydrophobic contact networks and the absence of Cβ-branched residues in a U-shaped loop (**Fig 4A**). The model was sufficiently stable in MD simulations of 10 ns (**Fig 4B**). We also created G127V mutant of PrP(107-143), PrP(107-143;G127V), and confirmed destabilizing effects of the mutation on the U-shaped loop (**Fig 4C and Supplementary Movie, PrP(107-143;G127V)**). To validate the instability, we used “proximity scores”, which represent sum total of frequency of hydrophobic contacts between two hydrophobic residues over ten chains A-J (**Supplementary Fig S2A**). The scores correlate with distances between them in certain cases (**Supplementary Fig S2B**) and also would reflect stability of the hydrophobic cores they contribute to. The significantly lower proximity scores for L125-L125 and V122-V122 of PrP(107-143;G127V) amyloid than those of WT (**Fig 4C, graph**) indicated that those residues are frequently wide apart, consistent with disordered U-shaped loops. Diagram of proximity scores of PrP(107-143;G127V) also revealed promiscuous hydrophobic interactions, reflecting the structural instability (**Supplementary Fig S2C, G127V**). The destabilization of the amyloid structure by G127V mutation was consistent with the protective effects of V127 polymorphism of human PrP against CJD transmission [36], because the destabilization would abolish propagation of the PrP^{Sc} in the brains.

Influences of M129V mutation on PrP(107-143) amyloid

Then, we analyzed influences of M129V substitution on stability of hydrophobic cores, which is equivalent to V129 polymorphism of human PrP. The mutant amyloid, PrP(107-143;M129V), appeared more stable during the 10 ns of simulation than the wild-type (**Fig 4D**). Comparison of their β-sheet propensity values validated the stability, with more demarcated loop(116-119) and smaller SD-β values in the region 129-134 (**Fig 4E, compare WT and M129V**). Incidentally, heat maps of PrP(107-143;G127V) further confirmed the disorder around the U-shaped loop (**Fig 4E, G127V**). Proximity scores of the wild-type and the mutant revealed more detailed differences (**Fig 4F**). Most notable was the alteration in the balances of interactions between A120, V122, L125 and V129 in hydrophobic cores of the U-shaped loops (**Fig 4F, upper left**). While the wild type showed outstandingly high proximity scores for V122-M129, M129V mutation significantly reduced the score and instead increased scores for V122-L125 and A120-V129, making the three scores almost even. Not significant but higher scores for A120-A120 and V129-V129 reflected more structural stability of the mutant amyloid. The mutation also

affected interactions in remote regions like those in the C-terminal region, i.e., significant increases in proximity scores for A116-F141, I139-I139 and F141-F141 (**Fig 4F, lower left**), and those in the more N-terminal region, i.e., significant increase and decrease in A113-V121 and A115-V121, respectively (**Fig 4F, lower right**). The altered interactions in the N-terminal region are particularly interesting because they are located on the other side from V129 across β-strand 120-122 and did not directly contact it; presumably, dynamics of β-sheet(120-122) was initially affected by the mutation and subsequently the interaction patterns of V121 were altered.

M129V mutation also increased proximity scores for A118-A133, although not statistically significant (**Fig 4F, upper right**) and the distances between β-sheet(120-122) and β-sheet(128-133) seemed to be narrower in the M129V mutant. Indeed, distances between Cα carbons of A118 and S132, δCα(118-132), tended to be shorter in mutants with M129V mutations (**Fig 5A, blue and green squares**) than in wild type (**black dots**). Interestingly, the wild type and mutants with M129 mostly had shorter δCα(118-133) than δCα(118-132), while the two distances of those with V129 were comparable (**Fig 5B, upper panels)**. There also was a certain correlation between δCα(120-129) and δCα(118-132) (**Fig 5B, lower panels and Fig 5C**) and mutants with V129 showed obviously shorter δCα(120-129) (**Fig 5C, blue and green squares**). All those findings were explainable by assuming a "upward" positional shift of β-sheet(128-133) in the mutants with V129 (**Fig 5D and 5E**) that is attributed to the shorter side chain of V129 than that of M129. The shortness enables V129 to further approach toward A120, consequently well-balanced interactions of the hydrophobic residues and closer positioning of the two β-sheets. Besides the local effects, the positional shift also expand the range of motion of the C-terminal region facilitating interactions of I139 and F141 with A116, although the increments of the proximity scores were not statistically significant (**Fig 4E, lower left**). On the other hand, with the long side chain of M129, biased interactions with V122 seem to hamper the approach of residue 129 toward A120.

Influences of A133V mutation on PrP(107-143) amyloid

V136 (in ovine numbering) is one of scrapie-prone polymorphisms of ovine PrP [39]. As the corresponding residue of human PrP, A133, faces the same direction as M129 in the present model (**Fig 4A**), we were interested in whether A133V mutation somehow affect structures of the PrP(107-143) amyloid. The mutant PrP(107-143;M133V) appeared to have β-sheet(120-122) and β-sheet(128-133) slightly wide apart than the wild type (**Fig 7A**), and similarly stable as the wild type overall (**Fig 7B**), as confirmed by the similar patterns of heat maps except for more demarcated loop(116-119) and very stable β-sheet propensity at residue 133 (**Fig 7C**). Consistent with the appearances, distances between Cα of residues 118 and 133 were very stably maintained at ~7 Å (**Fig 7D, Graph (A133V and WT)**) with significantly higher proximity scores for A118-V133 than that of WT (**Fig 7E, upper left**). Proximity scores of interactions of the C-terminal regions were also altered: the scores for A117-I139 were significantly increased along with significant decrease in the score for A116-I139 (**Fig 7E, upper right**). The scores for V122-M129 were also higher than those of the wild type although not statistically significant (**Fig 7E, lower panel**). Those alterations could be explained from the view point of the positional relations between β-sheet(120-122) and β-sheet(128-133) as discussed above (**Fig 5D and 5E**). In the A133V mutant, the stable A118-V133 relations fix positional relations of the two β-sheets at the status of the left panel of **Fig 5E**; the positional relation facilitates V122-M129 interactions and keeps I139 away from A116 due to the restricted motion range of the C-terminal region. The altered balance of the hydrophobic interactions by A133V mutation did not improve stability of the amyloid as much as M129V despite the stabilized relations of the two β-sheets. After all,

simulations of the present model did not provide any clue to the mechanism of how V136 of ovine PrP facilitates conversion.

Influences of I138M mutation on PrP(107-143) amyloids with or without M129V

Residue 138 is one of the residues that are often varied between species, e.g., Ile in human, Met in many rodents and Leu in many ruminants. It is the most influential on mouse-human species barrier in transmission of sCJD [40], and also in cross-seeding of Y145Stop peptides of human and mouse PrP [18]. We assessed how I138M mutation affect the local structural model of PrP^{Sc}. The most remarkable was the tendency of the C-terminal region leaning over toward the N-terminal region (**Fig 7A**), presumably due to bending at loop(134-137). Because of the bending, the angle between β-sheet(128-133) and β-sheet(139-141) appears to be near-square to acute in many of mutants with I138M, particularly in PrP(107-143;M129V;I138M) (**Supplementary Fig S3**), whereas the wild type or other mutants tend to have obtuse angles (**Fig 7A**). In comparison between PrP(107-143;I138M) and the wild type, β-sheet propensity (**Fig 7B**) or proximity scores (**Fig 7C**) were similar. Interestingly, proximity scores for A133-P137 are higher in the mutants with I138M (**Fig 7C, upper left**) and, in the runs with relatively high proximity scores for A133-P137 (**Fig 7D**), the amyloids tend to form small loops encompassing the two residues, like a Ω-shape (**Fig 7E, left panel**), and have near-square to acute angles between β-sheet(128-133) and β-sheet(139-141) irrespective of the primary structures (**Supplementary Fig S3, boxed ones**). The final shot of run 7 of PrP(107-143;M129V) (**Fig 4D**) also had high proximity score (**Fig 7D**). The deeper bending of the loop even to acute angles by the I138M mutation would be attributable to high intrinsic α-helix propensity of Met that increases freedom of motion of the loop and to the contact of two hydrophobic residues A133 and P137 which is thermodynamically favorable. In this particular conformation, V129 seems rather compatible with M138: the "upward shift" of β-sheet(128-133) brings A133 to a position where P137 can efficiently interact and allowed loop(134-137) to bend deeper without the C-terminal region colliding against loop(116-118). On the other hand, in those with M129, the deeper bending is not allowed to the full extent due to the steric clash. That may explain why the effects of I138M mutation is more accentuated in PrP(107-143;M129V;138M) than in PrP(107-143;I138M) (**Fig 7C**). For example, a significant difference in A120-A/V129 proximity scores was observed only between amyloids with V129, i.e., PrP(107-143;M129V) and PrP(107-143;M129V;I138M) (**Fig 7C, lower panel**). Possibly, efficient bending of loop(134-137) by M138 in PrP(107-143;M129V;138M) may facilitate further shift of β-sheet(128-133) to cause the difference, whereas the bending tend to be hampered in PrP(107-143;I138M) and the effects of M138 could not fully manifest. The same explanation holds true for the different proximity scores for A116-I139 (**Fig 7C, upper right**).

The behaviors of PrP(107-143;I138M) amyloid suggests what occurs in cross-seeding of mouse PrP or Syrian hamster PrP with human PrP^{Sc}, providing an potential insight into the mechanism of the species barrier. As Syrian hamster PrP has another Met at residue 139 which would make the region even more flexible, the region might make stably bent β-sheets as observed in αSyn(G84M) amyloid or the N-terminal region of PrP(107-143) encompassing 107-116.

Conclusion about the PrP(107-143) amyloid model

Collectively, the present model of local structure of PrP^{Sc} seems to be more compatible with V129 than with M129; this is an example of an amyloid conformation where differences of Met and Val affect the structural stability. The relative stability of the amyloid with V129 implies that human PrP with V129 may have this region as a

predominant N-terminal interface from which its conversion into PrP^{Sc} starts [41]. Another model which is more compatible with M129 than with V129 is underway. Designing such conformations solely based on the regional sequence could be difficult, if the M129-compatible local conformations depend on interactions with other regions for stability, as suggested by rather efficient transmission of M129-homozygous sporadic CJD to genetically-engineered mice expressing human-mouse chimeric PrP that have mouse sequences in the more C-terminal region [42][43].

Reinforcement of a single hydrophobic interaction between β-sheets by mutations, e.g., V122-M129 interaction in PrP(107-143;A133V) or A120-V129 interaction in PrP(107-143;M129V;I138M) amyloids, did not contribute to stabilization of the local structures. To the contrary, significantly lowered L125-L125 proximity scores of PrP(107-143;M129V;I138M) suggested a certain degree of destabilization of the β-arch by the alteration. Results of αSyn(G84M) and PrP(107-143;M129V) imply that well-balanced interactions of constituent residues in the hydrophobic core might be essential for maximal stability of a β-arch. If that is true, the number of patterns of β-arches that a single peptide can stably conform would be limited and that may underlie why types of PrP^{Sc} are limited in number.

Incidentally, the spontaneous approach of N- and C-termini of the amyloid which occurred in those with high A133-P137 proximity scores was notable, because those ends lead to positive- or negative-charge clusters, respectively, in a full-length human PrP. Those charged clusters can electrostatically interact and contribute to stabilization of the amyloid structures. It is interesting that the positive-charge cluster seems actually essential for structural conversion of the N-terminal region [44].

Knowledge from the present study may help design more plausible PrP^{Sc} models, local structural models of other regions of PrP^{Sc}, and other in-register parallel amyloids. For example, the region between the first and the second α-helixes of PrP, which is likely an interface between substrate PrP^{C} and template PrP^{Sc} on the C-terminal side [45], may also form a β-arch. Disulfide-crosslink scanning of mouse PrP and their conversion efficiencies by PrP^{Sc} of RML scrapie suggested that side chains of residue 165 and 166 (in mouse PrP numbering) are directed outward of a β-arch, forming a loop [46]. Because hydrophobic residues are sparse in the region, hydrogen bonds might be more important for reinforcement of the β-arch rather than hydrophobic effects. If the region PrP(107-143) is another PrP^{C}-PrP^{Sc} interface on the N-terminal side, the two native β-strands of PrP^{C}, β1 and β2, are comprised in a N- or C-terminal interface, respectively. It is conceivable that PrP^{Sc} initiates PrP^{C}-PrP^{Sc} conversion reactions by breaking the native β1-β2 anti-parallel sheet of PrP^{C} and snatching either one to incorporate into itself.

Potentially generally-applicable knowledge from the present studies

Unique effects of each group of hydrophobic amino acids in in-register parallel β-sheet amyloids are conformation-dependent, and attributable to Cβ branching and/or length of their side chains. Met and Ile showed similar influences in a flat loop of the αSyn amyloid, while Ile and Val in U-shaped loops destabilized the structures when they were not stably incorporated in hydrophobic cores. As the latter effects were observed in two different proteins, i.e., αSyn(G84I) and PrP(107-143;G127V), this notion may be generally applicable to other in-register parallel amyloids. In certain situations, Met can behave rather distinctly from other hydrophobic amino acids as in αSyn(G84M) amyloid where its long side chain stabilized the β-arch as a crossbeam across the arch forming a well-balanced interaction network. The long hydrophobic side chain of Met would be also advantageous for efficient inter-domain and inter-molecular interactions, as seen in an Aβ amyloid (PDB ID: 2mpz) [47]. However,

Met is not always advantageous for stable hydrophobic core formation as demonstrated in the tentative PrP(107-143) amyloid.

In terms of Cβ-branching and length of side chains, Val and Met can cause mutually rather different influences on β-arches and, if the β-arch constitutes an interface between substrate monomer and template amyloid, the differences cause species/strain barriers. The influences of polymorphism M/V129 of human PrP on phenotypes of prion diseases and susceptibilities to certain prion strains, e.g., new-variant CJD [7][8], might be explainable from this viewpoint.

Secondary Structure Prediction Algorithm: high α-helix propensity and β-sheet formation

We previously propounded that positions of β-sheets and loops of in-register parallel β-sheet amyloids could be predicted to some degree by the secondary structure prediction algorithm which conveniently assigns high Pα values to Ala and residues with long side chains without Cβ branching, e.g., Met and glutamine, and assigns high Pβ values to residues with intermediate-length side chains with Cβ branching, e.g., Val, Ile and threonine [24]. As presented above, regions with high α-helix propensities are compatible with β-sheet formation even when the backbone is bent, and may be actually advantageous for amyloid formation because of the adaptability to various shapes of β-arches. Even though an α-helix resists to conversion to a β-sheet due to requirement for the energy to unfold, it would stabilize β-arches once successfully converted. Hydrophilic residues with high α-helix propensity like glutamine can stabilize amyloids by making “glutamine ladders” [48]. Propensities around proline should be carefully interpreted, because the algorithm assigns too high coil propensities to proline than its actual effects on β-arches.

Limitation to the present Method

A caveat to our view is the artificial setting which starts with the same initial conformations irrespective of mutant types and suddenly unleashes them to move. In reality, higher freedom of motion of the backbone and potential steric effects of the long side chain of Met could hamper it settling into amyloid conformations. For example, spontaneous amyloid formation by Y145Stop mutant of Syrian-hamster PrP which has more Met than mouse or human PrP counterparts was inefficient [21]. Such inefficiency in folding into a conformation may divert a certain fraction of molecules to aberrant refolding pathways in in-vitro or in-vivo experiments. Regardless of the limitations, MD simulation provides a direct insight into structures and dynamics of in-register parallel β-sheet amyloids, and this approach can shed light on the mechanisms of strain diversity of amyloids including PrP^{Sc}.

Conclusion

We demonstrated how different groups of hydrophobic amino acids uniquely affect stability of U-shaped β-arches, and consequently the entire amyloid, in two different in-register parallel β-sheet amyloids. The studies also revealed how manifestation of effects of one mutation is affected by another mutation. The notion would be applicable to various in-register parallel β-sheet amyloids and other β-arches of PrP^{Sc}.

We expect that the knowledge from the present studies aid in designing more plausible PrP^{Sc} models and other amyloids in the future, and advance our understanding about in-register parallel β-sheet amyloids.

Materials and Methods

Detailed protocols of the modeling mutant αSyn amyloids, MD simulation, short MD simulation, and various

analyses were mostly the same as described in the preprint on bioRxiv [25]. Here we briefly describe essential points.

Secondary structure prediction

We used the same algorithm (http://cib.cf.ocha.ac.jp/bitool/MIX/) [32] as previously reported [24][33]. To clarify magnitude relations between two of the three conventional parameters, i.e., α-helix propensity (Pα), β-sheet propensity (Pβ), and coil propensity (Pc), we used their arithmetic differences as a new set of parameters, i.e., (Pβ-Pα), (Pβ-Pc) and (Pα-Pc) [24].

Modelling Structures of αSyn amyloids

We used a Greek-key αSyn amyloid (PDB ID: 2n0a [29]) as the starting structure, after truncating the disordered N- and C-terminal regions (residues 1–35 and 100–140, respectively) [25]. The N- and C-termini were acetylated and *N*-methylated using AmberTools16 [49]. For modelling αSyn mutants, we used SCWRL4 [50]. Modelled amyloids were solvated with a rhombic dodecahedron water box with a minimum wall distance of 12 Å using GROMACS (version 5.0.4). Na+ and Cl– ions were randomly placed to neutralize the system and yield a net concentration of 150 mM NaCl. The protonation state of the histidine at the residue 50 was fixed as the Nδ-H tautomer (HID form in AMBER naming convention) in all simulations.

MD simulations

GROMACS (versions 5.0.4 and 5.1.2) [51] with the AMBER ff99SB-ILDN force field [52] was used for MD simulations with the TIP3P water model [53]. The system was initially minimized for 5,000 steps with the steepest descent method, followed by 2,000 steps with the conjugate gradient method. During minimization, heavy atoms of the amyloids were restrained with a harmonic potential with a force constant of 10.0 kcal/mol•Å2. After minimization, the temperature of the system was increased from 0 to 310 K during a 1 ns simulation with the restraints. Next, a 1 ns equilibration run was performed by gradually removing the restraints from 10.0 kcal/mol•Å2 to zero and subsequent equilibration was performed in the NPT ensemble for 2 ns at 310 K and 1 bar. Production runs were carried out for 400 ns in the NPT ensemble at 310 K and 1 bar (**Supplementary Figure S1A**). We used the velocity-rescaling scheme [54] and the Berendsen scheme [55] for thermostat and barostat, respectively. The LINCS algorithm [56] was used to constrain all bonds with hydrogen atoms, allowing the use of a 2 fs time step. Electrostatic interactions were calculated with the Particle-mesh Ewald method [57]. The cut-off length was set to 12 Å for Coulomb and van der Waals interactions. The Verlet cut-off scheme [58] was used for neighbour searching. Trajectory snapshots were saved every 10 ps for the MD simulations.

Analyses

As for analyses of 400-ns simulations, the first 100 ns of each MD trajectory was discarded, and 30,001 snapshots (trajectory from 100 to 400 ns) were used. The secondary structure content during the simulations was calculated using DSSP [59,60] and gmx do_dssp in GROMACS. Hydrophobic contacts were analysed using PyInteraph [61]. A hydrophobic contact was assigned if the distance between the centres of mass of side chains is less than 5 Å [62][63]. The results of hydrophobic contact analyses were visualized using Cytoscape (version 3.5.1) [64]. All molecular structures for αSyn amyloids were drawn by UCSF Chimera (version 1.12) [65] and Swiss PDB Viewer [66]. The movies of trajectories of MD simulations were prepared with VMD [67].

Short MD runs

We carried out 5 ns production runs from the common minimized structure according to the almost same

procedure as the 400 ns MD simulations. For the simulation of αSyn(G84L), αSyn(G84I) and αSyn(G84V) amyloids, the initial structures were modeled by replacing Met84 of an energy-minimized αSyn(G84M) amyloid by using SCWRL4 [50] (**Supplementary Figure S1B**). We carried out 5 MD simulations for αSyn(G84M), αSyn(G84L), αSyn(G84I) and αSyn(G84V), and 30 MD simulations for αSyn(G84F) and αSyn(G84A).

Modeling PrP(107-143) amyloids and MD simulations

In designing local structural models of human PrP^{Sc}, we adopted the region comprising -$GGL_{125}GG$- as denoted above and decided the N-terminus and the C-terminus of the peptide to avoid charged residues at the ends because they can excessively destabilize in-register parallel β-sheet structures particularly when they are at the free ends. As there are a positive- and a negative-charge clusters in the regions 101-106 and 144-147, respectively, the region between them was used for the modeling. First, we roughly designed conformations of a single layer of amyloid with Swiss PDB viewer [66], then piled it up to make an in-register parallel β-sheet amyloid with UCSF Chimera [65]. The model amyloids with 10 layers were refined using Modeller (version 9.15) [68] with β-sheet restraints for the residues A120-V122, Y128-L130, and I138-F141. The N- and C-termini of the refined models were acetylated and *N*-methylated using PyMOL [69] and mutants were generated by using SCWRL4 [50]. We carried out 10 runs of 10 ns MD simulations for each model with almost the same procedure as the 400 ns MD simulations (**Supplementary Figure S1C**). The trajectories of the production runs were used for analysis described in *Analyses* section.

Statistical analyses

Two-tailed Welch two sample t-test was used for analysis of statistical differences between two groups. A p-value less than 0.05 was considered statistically significant. The approximation lines were determined by ordinary least square on values from the independent ten runs of simulations.

Acknowledgement

We thank Kei Yura, Ochanomizu University, for generously allowing us to use the neural network secondary structure prediction algorithm on his website. The numerical calculations were carried out on the TSUBAME2.5/3.0 supercomputer at the Tokyo Institute of Technology and the Reedbush-U supercomputer at the Information Technology Center, the University of Tokyo. This work was supported by the "TSUBAME Encouragement Program for Young/Female Users" of Global Scientific Information and Computing Center at the Tokyo Institute of Technology, the “Initiative on Promotion of Supercomputing for Young or Women Researchers” from the Information Technology Center, the University of Tokyo, Takeda Science Foundation (www.takeda-sci.or.jp/), and JSPS KAKENHI Grant Numbers 19K16058 (to HO) and 19K22539 (to YT).

References

1. Prusiner, S.B. Prions. *Proc. Natl. Acad. Sci. U. S. A.* **1998**, *95*, 13363–13383, doi:10.1073/pnas.95.23.13363.
2. Hope, J.; Reekie, L.J.D.; Hunter, N.; Multhaup, G.; Beyreuther, K.; White, H.; Scott, A.C.; Stack, M.J.; Dawson, M.; Wells, G.A.H. Fibrils from brains of cows with new cattle disease contain scrapie-associated protein. *Nature* **1988**, *336*, 390–392, doi:10.1038/336390a0.
3. Williams, E.S. Chronic Wasting Disease. *Vet. Pathol.* **2005**, *549*, 530–549, doi:10.1354/vp.42-5-530.
4. Telling, G.C.; Parchi, P.; DeArmond, S.J.; Cortelli, P.; Montagna, P.; Gabizon, R.; Mastrianni, J.; Lugaresi, E.; Gambetti, P.; Prusiner, S.B. Evidence for the conformation of the pathologic isoform of the prion protein enciphering and propagating prion diversity. *Science* **1996**, *274*, 2079–82.
5. Parchi, P.; Giese, A.; Capellari, S.; Brown, P.; Schulz-Schaeffer, W.; Windl, O.; Zerr, I.; Budka, H.; Kopp, N.; Piccardo, P.; Poser, S.; Rojiani, A.; Streichemberger, N.; Julien, J.; Vital, C.; Ghetti, B.; Gambetti, P.; Kretzschmar, H. Classification of sporadic Creutzfeldt-Jakob disease based on molecular and phenotypic analysis of 300 subjects. *Ann. Neurol.* **1999**, *46*, 224–33.
6. Goldfarb, L.G.; Petersen, R.B.; Tabaton, M.; Brown, P.; LeBlanc, A.C.; Montagna, P.; Cortelli, P.; Julien, J.; Vital, C.; Pendelbury, W.W. Fatal familial insomnia and familial Creutzfeldt-Jakob disease: disease phenotype determined by a DNA polymorphism. *Science* **1992**, *258*, 806–8.
7. Collinge, J.; Beck, J.; Campbell, T.; Estibeiro, K.; Will, R.G. Prion protein gene analysis in new variant cases of Creutzfeldt-Jakob disease. *Lancet* **1996**, *348*, 56, doi:https://doi.org/10.1016/S0140-6736(05)64378-4.
8. Collinge, J. Molecular neurology of prion disease. *J. Neurol. Neurosurg. Psychiatry* **2005**, *76*, 906–919, doi:10.1136/jnnp.2004.048660.
9. Green, K.M.; Browning, S.R.; Seward, T.S.; Jewell, J.E.; Ross, D.L.; Green, M.A.; Williams, E.S.; Hoover, E.A.; Telling, G.C. The elk PRNP codon 132 polymorphism controls cervid and scrapie prion propagation. *J. Gen. Virol.* **2008**, *89*, 598–608, doi:10.1099/vir.0.83168-0.
10. Hamir, A.N.; Gidlewski, T.; Spraker, T.R.; Miller, J.M.; Creekmore, L.; Crocheck, M.; Cline, T.; O'Rourke, K.I. Preliminary observations of genetic susceptibility of elk (Cervus elaphus nelsoni) to chronic wasting disease by experimental oral inoculation. *J. Vet. Diagn. Invest.* **2006**, *18*, 110–4.
11. Vázquez-fernández, E.; Vos, M.R.; Afanasyev, P.; Cebey, L.; Sevillano, A.M.; Vidal, E.; Rosa, I.; Renault, L.; Ramos, A.; Peters, P.J.; Fernández, J.J.; Heel, M. van; Young, H.S.; Requena, J.R.; Wille, H. The Structural Architecture of an Infectious Mammalian Prion Using Electron Cryomicroscopy. *PLoS Pathog.* **2016**, *12*, e1005835, doi:10.1371/journal.ppat.1005835.
12. Silva, C.J.; Vázquez-Fernández, E.; Onisko, B.; Requena, J.R. Proteinase K and the structure of PrPSc: The good, the bad and the ugly. *Virus Res.* **2015**, *207*, 120–126, doi:10.1016/j.virusres.2015.03.008.
13. Tycko, R.; Savtchenko, R.; Ostapchenko, V.G.; Makarava, N.; Baskakov, I. V The α-helical C-terminal domain of full-length recombinant PrP converts to an in-register parallel β-sheet structure in PrP fibrils: evidence from solid state nuclear magnetic resonance. *Biochemistry* **2010**, *49*, 9488–97, doi:10.1021/bi1013134.
14. Groveman, B.R.; Dolan, M.A.; Taubner, L.M.; Kraus, A.; Wickner, R.B.; Caughey, B. Parallel in-register intermolecular β-sheet architectures for prion-seeded prion protein (PrP) amyloids. *J. Biol. Chem.* **2014**,

289, 24129–24142, doi:10.1074/jbc.M114.578344.

15. Cobb, N.J.; Sönnichsen, F.D.; McHaourab, H.; Surewicz, W.K. Molecular architecture of human prion protein amyloid: a parallel, in-register beta-structure. *Proc. Natl. Acad. Sci. U. S. A.* **2007**, *104*, 18946–51, doi:10.1073/pnas.0706522104.
16. Theint, T.; Xia, Y.; Nadaud, P.S.; Mukhopadhyay, D.; Schwieters, C.D.; Surewicz, K.; Surewicz, W.K.; Jaroniec, C.P. Structural Studies of Amyloid Fibrils by Paramagnetic Solid-State Nuclear Magnetic Resonance Spectroscopy. *J. Am. Chem. Soc.* **2018**, *140*, 13161–13166, doi:10.1021/jacs.8b06758.
17. Priola, S.A.; Chesebro, B. A Single Hamster PrP Amino Acid Blocks Conversion to Protease-Resistant PrP in Scrapie-Infected Mouse Neuroblastoma Cells. *J. Virol.* **1995**, *69*, 7754–7758.
18. Vanik, D.L.; Surewicz, K.A.; Surewicz, W.K. Molecular basis of barriers for interspecies transmissibility of mammalian prions. *Mol. Cell* **2004**, *14*, 139–145, doi:10.1016/S1097-2765(04)00155-8.
19. Giles, K.; De Nicola, G.F.; Patel, S.; Glidden, D. V; Korth, C.; Oehler, A.; DeArmond, S.J.; Prusiner, S.B. Identification of I137M and other mutations that modulate incubation periods for two human prion strains. *J. Virol.* **2012**, *86*, 6033–41, doi:10.1128/JVI.07027-11.
20. Lowenstein, D.H.; Butler, D. a; Westaway, D.; McKinley, M.P.; DeArmond, S.J.; Prusiner, S.B. Three hamster species with different scrapie incubation times and neuropathological features encode distinct prion proteins. *Mol. Cell. Biol.* **1990**, *10*, 1153–1163, doi:10.1128/MCB.10.3.1153.Updated.
21. Meade-White, K.D.; Barbian, K.D.; Race, B.; Favara, C.; Gardner, D.; Taubner, L.; Porcella, S.; Race, R. Characteristics of 263K scrapie agent in multiple hamster species. *Emerg. Infect. Dis.* **2009**, *15*, 207–215, doi:10.3201/eid1502.081173.
22. Shirai, T.; Saito, M.; Kobayashi, A.; Asano, M.; Hizume, M.; Ikeda, S.; Teruya, K.; Morita, M.; Kitamoto, T. Evaluating Prion Models Based on Comprehensive Mutation Data of Mouse PrP. *Structure* **2014**, 1–12, doi:10.1016/j.str.2013.12.019.
23. Harrathi, C.; Fernández-borges, N.; Eraña, H.; Elezgarai, S.R.; Venegas, V.; Charco, J.M.; Castilla, J. Insights into the Bidirectional Properties of the Sheep – Deer Prion Transmission Barrier. *Mol. Neurobiol.* **2019**, *56*, 5287–5303, doi:10.1007/s12035-018-1443-8.
24. Taguchi, Y.; Otaki, H.; Nishida, N. Mechanisms of Strain Diversity of Disease-Associated in-Register Parallel β-Sheet Amyloids and Implications About Prion Strains Yuzuru. *Viruses* **2019**, *11*, doi:10.3390/v11020110.
25. Otaki, H.; Taguchi, Y.; Nishida, N. Molecular dynamics simulation reveals that switchable combinations of β-sheets underlie the prion-like properties of α-synuclein amyloids. *bioRxiv* **2018**, doi:https://doi.org/10.1101/326462.
26. Melki, R. Alpha-synuclein and the prion hypothesis in Parkinson's disease. *Rev. Neurol. (Paris).* **2018**, 1–9, doi:10.1016/j.neurol.2018.08.002.
27. Bousset, L.; Pieri, L.; Ruiz-arlandis, G.; Gath, J.; Jensen, P.H.; Habenstein, B.; Madiona, K.; Olieric, V.; Böckmann, A.; Meier, B.H.; Melki, R. Structural and functional characterization of two alpha-synuclein strains. *Nat. Commun.* **2013**, *4*, 2575, doi:10.1038/ncomms3575.
28. Peng, C.; Gathagan, R.J.; Covell, D.J.; Medellin, C.; Stieber, A.; Robinson, J.L.; Zhang, B.; Pitkin, R.M.; Olufemi, M.F.; Luk, K.C.; Trojanowski, J.Q.; Lee, V.M.Y. Cellular milieu imparts distinct pathological

α-synuclein strains in α-synucleinopathies. *Nature* **2018**, *557*, 558–563, doi:10.1038/s41586-018-0104-4.

29. Tuttle, M.D.; Comellas, G.; Nieuwkoop, A.J.; Covell, D.J.; Berthold, D.A.; Kloepper, K.D.; Courtney, J.M.; Kim, J.K.; Barclay, A.M.; Kendall, A.; Wan, W.; Stubbs, G.; Schwieters, C.D.; Lee, V.M.Y.; George, J.M.; Rienstra, C.M. Solid-State NMR Structure of a Pathogenic Fibril of Full-Length Human α-Synuclein. *Nat. Struct. Mol. Biol.* **2016**, *23*, 409–415, doi:10.1038/nsmb.3194.Solid-State.
30. Li, B.; Ge, P.; Murray, K.A.; Sheth, P.; Zhang, M.; Nair, G.; Sawaya, M.R.; Shin, W.S.; Boyer, D.R.; Ye, S.; Eisenberg, D.S.; Zhou, Z.H.; Jiang, L. Cryo-EM of full-length α-synuclein reveals fibril polymorphs with a common structural kernel. *Nat. Commun.* **2018**, *9*, 3609, doi:10.1038/s41467-018-05971-2.
31. Guerrero-Ferreira, R.; Taylor, N.M.; Mona, D.; Ringler, P.; Lauer, M.E.; Riek, R.; Britschgi, M.; Stahlberg, H. Cryo-EM structure of alpha-synuclein fibrils. *Elife* **2018**, *7*, e36402, doi:10.7554/eLife.36402.
32. Qian, N.; Sejnowski, T.J. Predicting the secondary structure of globular proteins using neural network models. *J. Mol. Biol.* **1988**, *202*, 865–884, doi:10.1016/0022-2836(88)90564-5.
33. Taguchi, Y.; Nishida, N. Secondary-structure prediction revisited□: Theoretical β -sheet propensity and coil propensity represent structures of amyloids and aid in elucidating phenomena involved in interspecies transmission of prions. *PLoS One* **2017**, *12*, e0171974, doi:10.1371/journal.pone.0171974.
34. Lyu, P.C.; Sherman, J.C.; Chen, A.; Kallenbach, N.R. *Alpha-helix stabilization by natural and unnatural amino acids with alkyl side chains.*; 1991; Vol. 88;.
35. Berg, J.; Tymoczko, J.; Stryer, L. The Amino Acid Sequence of a Protein Determines Its Three-Dimensional Structure. In *Biochemistry*; New York: W H Freeman, 2002.
36. Asante, E.A.; Smidak, M.; Grimshaw, A.; Houghton, R.; Tomlinson, A.; Jeelani, A.; Jakubcova, T.; Hamdan, S.; Richard-Londt, A.; Linehan, J.M.; Brandner, S.; Alpers, M.; Whitfield, J.; Mead, S.; Wadsworth, J.D.F.; Collinge, J. A naturally occurring variant of the human prion protein completely prevents prion disease. *Nature* **2015**, *522*, 478–81, doi:10.1038/nature14510.
37. Theint, T.; Nadaud, P.S.; Aucoin, D.; Helmus, J.J.; Pondaven, S.P.; Surewicz, K.; Surewicz, W.K.; Jaroniec, C.P. Species-dependent structural polymorphism of Y145Stop prion protein amyloid revealed by solid-state NMR spectroscopy. *Nat. Commun.* **2017**, *8*, 753, doi:10.1038/s41467-017-00794-z.
38. Choi, J.; Cali, I.; Surewicz, K.; Kong, Q.; Gambetti, P.; Surewicz, W.K. Amyloid fibrils from the N-terminal prion protein fragment are infectious. *Proc. Natl. Acad. Sci. U. S. A.* **2016**, *113*, 13851–13856, doi:10.1073/pnas.1610716113.
39. Goldmann, W.; Hunter, N.; Smith, G.; Foster, J.; Hope, J. PrP genotype and agent effects in scrapie: Change in allelic interaction with different isolates of agent in sheep, a natural host of scrapie. *J. Gen. Virol.* **1994**, *75*, 989–995, doi:10.1099/0022-1317-75-5-989.
40. Giles, K.; De Nicola, G.F.; Patel, S.; Glidden, D. V.; Korth, C.; Oehler, a.; DeArmond, S.J.; Prusiner, S.B. Identification of I137M and Other Mutations That Modulate Incubation Periods for Two Human Prion Strains. *J. Virol.* **2012**, *86*, 6033–6041, doi:10.1128/JVI.07027-11.
41. Taguchi, Y.; Schätzl, H.M. Identifying critical sites of PrPc -PrPSc interaction in prion-infected cells by dominant-negative inhibition. *Prion* **2013**, *7*, 1–5.
42. Taguchi, Y.; Mohri, S.; Ironside, J.W.; Muramoto, T.; Kitamoto, T. Humanized knock-in mice expressing chimeric prion protein showed varied susceptibility to different human prions. *Am. J. Pathol.* **2003**, *163*,

2585–2593, doi:10.1016/S0002-9440(10)63613-9.

43. Korth, C.; Kaneko, K.; Groth, D.; Heye, N.; Telling, G.; Mastrianni, J.; Parchi, P.; Gambetti, P.; Will, R.; Ironside, J.; Heinrich, C.; Tremblay, P.; DeArmond, S.J.; Prusiner, S.B. Abbreviated incubation times for human prions in mice expressing a chimeric mouse-human prion protein transgene. *Proc. Natl. Acad. Sci. U. S. A.* **2003**, *100*, 4784–9, doi:10.1073/pnas.2627989100.

44. Groveman, B.R.; Raymond, G.J.; Campbell, K.J.; Race, B.; Raymond, L.D.; Hughson, A.G.; Orrú, C.D.; Kraus, A.; Phillips, K.; Caughey, B. Role of the central lysine cluster and scrapie templating in the transmissibility of synthetic prion protein aggregates. *PLoS Pathog.* **2017**, *13*, e1006623, doi:10.1371/journal.ppat.1006623.

45. Taguchi, Y.; Mistica, A.M. a; Kitamoto, T.; Schätzl, H.M. Critical significance of the region between Helix 1 and 2 for efficient dominant-negative inhibition by conversion-incompetent prion protein. *PLoS Pathog.* **2013**, *9*, e1003466, doi:10.1371/journal.ppat.1003466.

46. Taguchi, Y.; Lu, L.; Marrero-Winkens, C.; Otaki, H.; Nishida, N.; Schatzl, H.M. Disulfide-crosslink scanning reveals prion–induced conformational changes and prion strain–specific structures of the pathological prion protein PrPSc(J. Biol. Chem. (2018) 293, 38 (12730-12740) DOI:10.1074/jbc.RA117.001633). *J. Biol. Chem.* **2018**, *293*, 14925, doi:10.1074/jbc.AAC118.005526.

47. Sgourakis, N.G.; Yau, W.M.; Qiang, W. Modeling an in-register, parallel “iowa” Aβ fibril structure using solid-state NMR data from labeled samples with Rosetta. *Structure* **2015**, *23*, 216–227, doi:10.1016/j.str.2014.10.022.

48. Kurt, T.D.; Aguilar-Calvo, P.; Jiang, L.; Rodriguez, J.A.; Alderson, N.; Eisenberg, D.S.; Sigurdson, C.J. Asparagine and glutamine ladders promote cross-species prion conversion. *J. Biol. Chem.* **2017**, *292*, 19076–19086, doi:10.1074/jbc.M117.794107.

49. Case, D.A.; Betz, R.M.; Cerutti, D.S.; Cheatham, III, T.E.; Darden, T.A.; Duke, R.E.; Giese, T.J.; Gohlke, H.; Goetz, A.W.; Homeyer, N.; Izadi, S.; Janowski, P.; Kaus, J.; Kovalenko, A.; Lee, T.S.; LeGrand, S.; Li, P.; Lin, C.; Luchko, T.; Luo, R.; Madej, B.; Mermelstein, D.; Merz, K.M.; Monard, G.; Nguyen, H.; Nguyen, H.T.; Omelyan, I.; Onufriev, A.; Roe, D.R.; Roitberg, A.; Sagui, C.; Simmerling, C.L.; Botello-Smith, W.M.; Swails, J.; Walker, R.C.; Wang, J.; Wolf, R.M.; Wu, X.; Xiao, L.; Kollman, P.A. *AmberTools16. University of California, San Francisco.*; 2016;

50. Krivov, G.G.; Shapovalov, M. V; Dunbrack, R.L. Improved prediction of protein side-chain conformations with SCWRL4. *Proteins Struct. Funct. Bioinforma.* **2009**, *77*, 778–795, doi:10.1002/prot.22488.

51. Abraham, M.J.; Murtola, T.; Schulz, R.; Páll, S.; Smith, J.C.; Hess, B.; Lindahl, E. GROMACS: High performance molecular simulations through multi-level parallelism from laptops to supercomputers. *SoftwareX* **2015**, *1–2*, 19–25, doi:https://doi.org/10.1016/j.softx.2015.06.001.

52. Lindorff-Larsen, K.; Piana, S.; Palmo, K.; Maragakis, P.; Klepeis, J.L.; Dror, R.O.; Shaw, D.E. Improved side-chain torsion potentials for the Amber ff99SB protein force field. *Proteins Struct. Funct. Bioinforma.* **2010**, *78*, 1950–1958, doi:10.1002/prot.22711.

53. Jorgensen, W.L.; Chandrasekhar, J.; Madura, J.D.; Impey, R.W.; Klein, M.L. Comparison of simple potential functions for simulating liquid water. *J. Chem. Phys.* **1983**, *79*, 926–935, doi:10.1063/1.445869.

54. Bussi, G.; Donadio, D.; Parrinello, M. Canonical sampling through velocity rescaling. *J. Chem. Phys.* **2007**,

126, 14101, doi:10.1063/1.2408420.

55. Berendsen, H.J.C.; Postma, J.P.M.; van Gunsteren, W.F.; DiNola, A.; Haak, J.R. Molecular dynamics with coupling to an external bath. *J. Chem. Phys.* **1984**, *81*, 3684–3690, doi:10.1063/1.448118.
56. Hess, B. P-LINCS: A Parallel Linear Constraint Solver for Molecular Simulation. *J. Chem. Theory Comput.* **2008**, *4*, 116–122, doi:10.1021/ct700200b.
57. Essmann, U.; Perera, L.; Berkowitz, M.L.; Darden, T.; Lee, H.; Pedersen, L.G. A smooth particle mesh Ewald method. *J. Chem. Phys.* **1995**, *103*, 8577–8593, doi:10.1063/1.470117.
58. Páll, S.; Hess, B. A flexible algorithm for calculating pair interactions on SIMD architectures. *Comput. Phys. Commun.* **2013**, *184*, 2641–2650, doi:https://doi.org/10.1016/j.cpc.2013.06.003.
59. Touw, W.G.; Baakman, C.; Black, J.; te Beek, T.A.H.; Krieger, E.; Joosten, R.P.; Vriend, G. A series of PDB-related databanks for everyday needs. *Nucleic Acids Res.* **2015**, *43*, D364–D368, doi:10.1093/nar/gku1028.
60. Kabsch, W.; Sander, C. Dictionary of protein secondary structure: Pattern recognition of hydrogen-bonded and geometrical features. *Biopolymers* **1983**, *22*, 2577–2637, doi:10.1002/bip.360221211.
61. Tiberti, M.; Invernizzi, G.; Lambrughi, M.; Inbar, Y.; Schreiber, G.; Papaleo, E. PyInteraph: A Framework for the Analysis of Interaction Networks in Structural Ensembles of Proteins. *J. Chem. Inf. Model.* **2014**, *54*, 1537–1551, doi:10.1021/ci400639r.
62. Salamanca Viloria, J.; Allega, M.F.; Lambrughi, M.; Papaleo, E. An optimal distance cutoff for contact-based Protein Structure Networks using side-chain centers of mass. *Sci. Rep.* **2017**, *7*, 2838, doi:10.1038/s41598-017-01498-6.
63. Tiberti, M.; Invernizzi, G.; Lambrughi, M.; Inbar, Y.; Schreiber, G.; Papaleo, E. PyInteraph: A framework for the analysis of interaction networks in structural ensembles of proteins. *J. Chem. Inf. Model.* **2014**, *54*, 1537–1551, doi:10.1021/ci400639r.
64. Shannon, P.; Markiel, A.; Ozier, O.; Baliga, N.S.; Wang, J.T.; Ramage, D.; Amin, N.; Schwikowski, B.; Ideker, T. Cytoscape: A Software Environment for Integrated Models of Biomolecular Interaction Networks. *Genome Res.* **2003**, *13*, 2498–2504, doi:10.1101/gr.1239303.
65. Pettersen, E.F.; Goddard, T.D.; Huang, C.C.; Couch, G.S.; Greenblatt, D.M.; Meng, E.C.; Ferrin, T.E. UCSF Chimera—A visualization system for exploratory research and analysis. *J. Comput. Chem.* **2004**, *25*, 1605–1612, doi:10.1002/jcc.20084.
66. Guex, N.; Peitsch, M.C. SWISS-MODEL and the Swiss-PdbViewer: An environment for comparative protein modeling. *Electrophoresis* **1997**, *18*, 2714–2723, doi:10.1002/elps.1150181505.
67. Humphrey, W.; Dalke, A.; Schulten, K. VMD: Visual molecular dynamics. *J. Mol. Graph.* **1996**, *14*, 33–38, doi:https://doi.org/10.1016/0263-7855(96)00018-5.
68. Šali, A.; Blundell, T.L. Comparative protein modelling by satisfaction of spatial restraints. *J. Mol. Biol.* 1993, *234*, 779–815.
69. DeLano, W.L. PyMOL: An open-source molecular graphics tool. CCP4 Newsl. *Protein Crystallogr.* **2002**, *40*, 82–92.

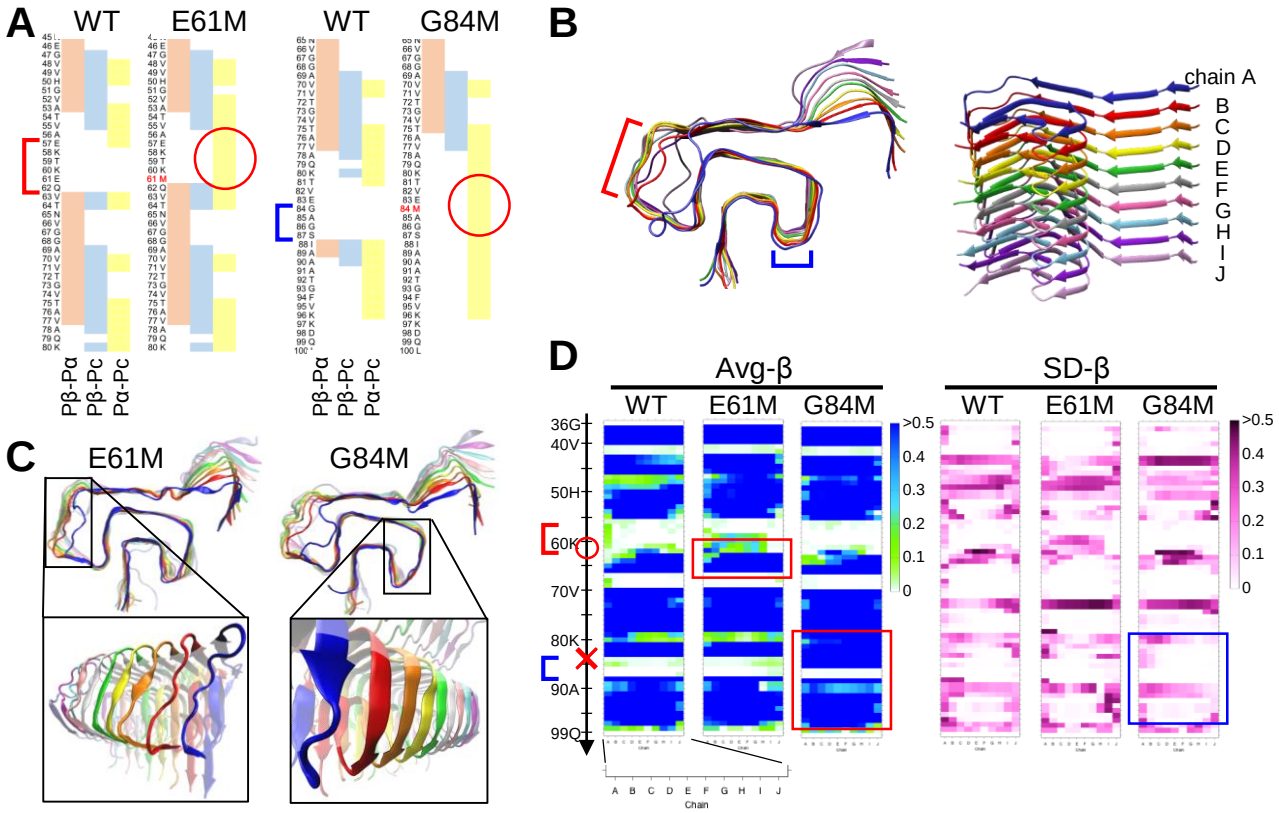

Fig 1. Influences of methionine (Met) substitutions on local structures of the "Greek-key" αSyn amyloid.
A. Secondary structure predictions profiles of αSyn(E61M) and αSyn(G84M), showing the magnitude relations between Pα, Pβ, and Pc, i.e., Pβ-Pα, Pβ-Pc, and Pα-Pc; residues with zero ("0") or positive values are indicated in red, blue and yellow, respectively. E61M and G84M substitutions are indicated in red letters. WT, wild-type αSyn. Red and blue brackets indicate positions of loop(57-62) and loop(84-87), respectively.
B. A final snapshot of αSyn(WT) after 400 ns of MD simulation of a "Greek-key" αSyn amyloid (PDB ID: 2n0a) (left). Red and blue brackets indicate the loops in Fig 1A. Chains of the amyloid stack are referred to as chain A-J (right).
C. Final shots of αSyn(E61M) (left) and αSyn(G84M) (right) amyloids after 400 ns of MD simulations. The insets view the indicated regions from slightly different angles to show each chain. Note that β-sheets are induced in loop(57-62) of αSyn(E61M) amyloid (left inset), and αSyn(G84M) amyloid has β-sheets extended to loop(84-87) (right inset).
D. Heatmaps of the average β-sheet propensity values (Avg-β) and the standard deviations of the values (SD-β) based on five (for WT) and three (for the mutants) independent runs of 400-ns MD simulations. Vertical axes and horizontal axes of all the heatmaps represent the residue numbers and the chains A-J, respectively. Red circle and cross on the vertical axis indicates positions of E61M and G84M, respectively. Avg-β values in loop(57-62) of αSyn(E61M) and in loop(84-87) of αSyn(G84M) amyloids were increased (red boxes) corresponding to the induced β-sheets in those regions (Fig 1B). The relatively low SD-β values in αSyn(G84M) amyloid (blue box) reflect the stabilized local structures.

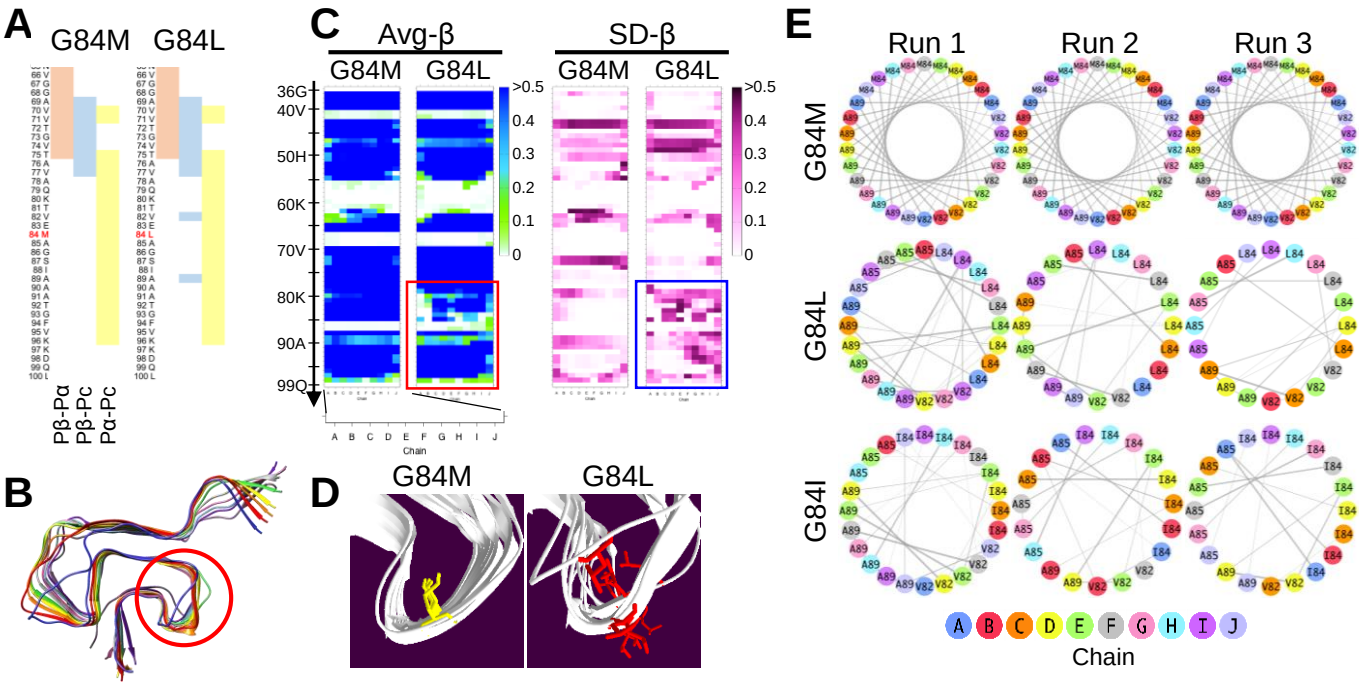

Fig 2. Influences of G84L and G84M are different despite their hydrophobicity and the absence of Cβ-branching in common.

A. Secondary structure prediction profiles of αSyn(G84L) in comparison with αSyn(G84M).

B. A final snapshot of αSyn(G84L) amyloid after 400 ns of MD simulation. The local structures around the mutation were disturbed (red circle).

C. Heat maps of Avg-β and SD-β of αSyn(G84L) amyloid based on three independent runs of 400 ns, which reflect the structural disturbances by the mutation (red and blue boxes).

D. Directions of the side chains of residue 84 after 400 ns of simulation. Some side chains of L84 are pointing outward, while those of M84 stay inside.

E. Hydrophobic contact diagrams based on simulation of 400 ns. Only the residues involved in the interactions with residue 84 are presented. Residue numbers and chains are indicated by numbers and colors of the dots, respectively. Thickness of each line corresponds to occupancy of the hydrophobic contact.

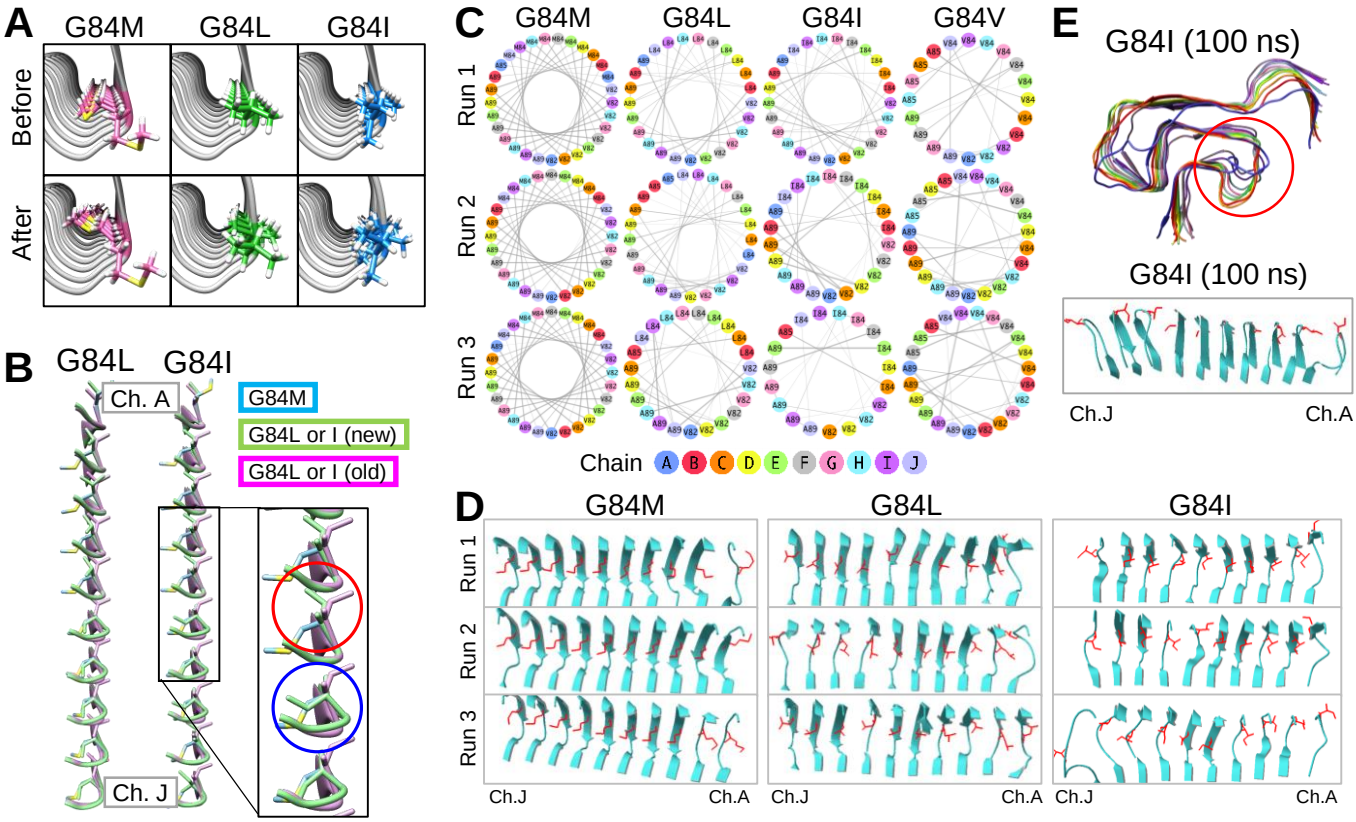

Fig 3. The different results among αSyn(G84M), αSyn(G84L) and αSyn(G84I) amyloids are not due to differences in their initial status.

A. Status of the three mutant αSyn amyloids before and after energy-minimization step.

B. Side views of the status of side chains of Leu84 and Ile84 after modeling by a software SCWRL4, comparing a modeling based on αSyn(WT) ("G84L or I (old)", purple chains) and another based on the energy-minimized αSyn(G84M) amyloid ("G84L or I (new)", green chains). Only residues 83-85 are shown.

C. Hydrophobic contact diagrams of mutant αSyn amyloids based on short MD simulations of 5 ns, after modeling based on the energy-minimized αSyn(G84M) amyloid. Only the residues involved in the interactions with residue 84 are presented.

D. Final shots of the mutant αSyn amyloids of the same short-MD simulations as in Fig 3C, showing directions of the side chains of residues 84 in red. Only the region from Lys80 to Ala90 is shown. Note that the side chains of M84 mostly maintained the same positions and directions as in the initial status, whereas those of L84 and I84 point different directions with some even flipping and local β-sheet structures were lost.

E. A final shot of αSyn(G84I) amyloid after the 5-ns simulation Run 1 was extended up to 100 ns (upper panel), and status of the side chains of I84 (lower panel). The loop region was viewed from outside of the β-arch to show flipping of the side chains.

Figure 4

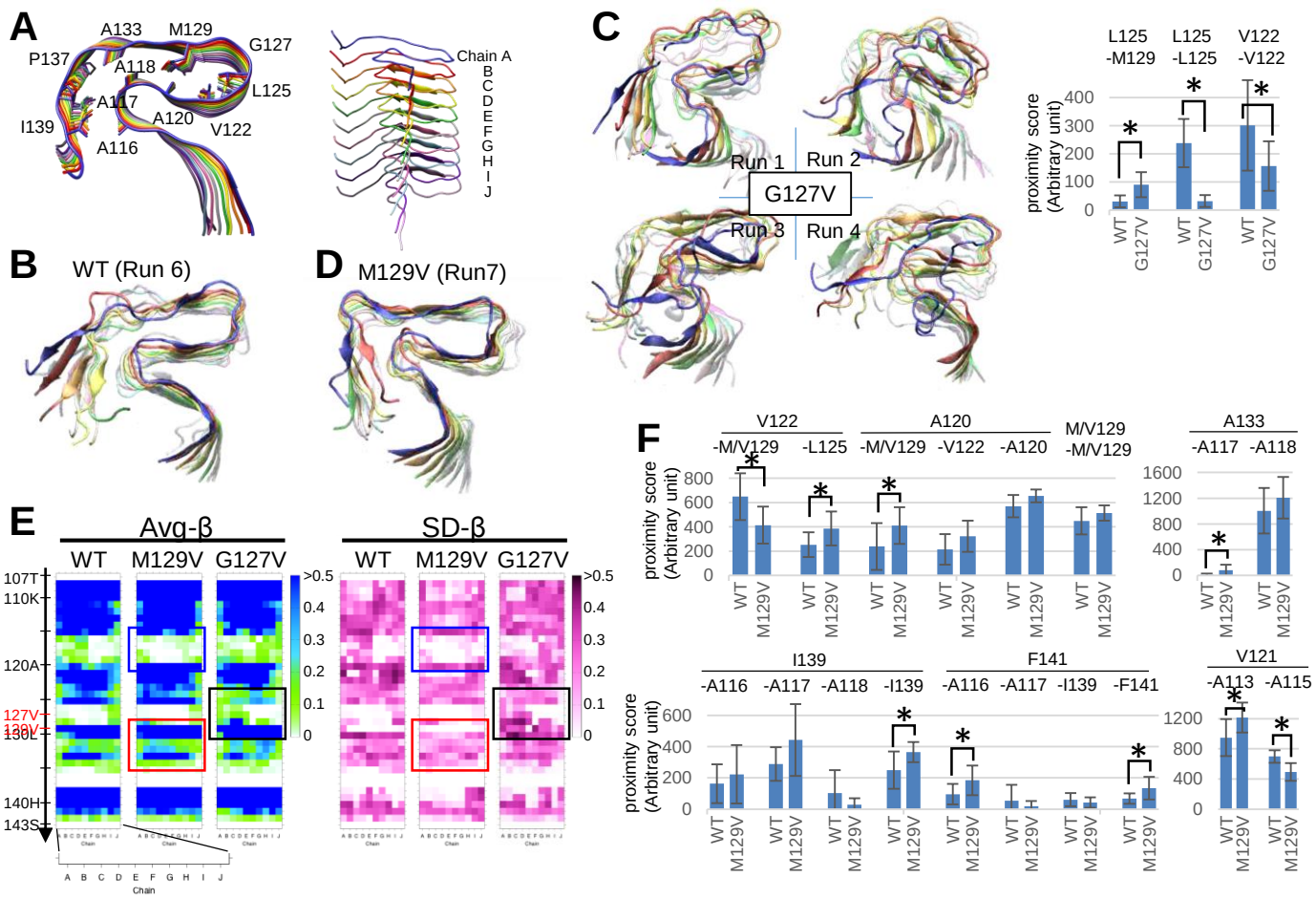

Fig 4. Influences of G127V and M129V mutations on a local structural model of human PrP^{Sc} encompassing 107-143

A. A PrP(107-143) amyloid as a tentative local-structural model of PrP^{Sc} and an oblique view showing the ten layers (Chain A-J). Side chains of residues that are mentioned later are annotated.

B. A final shot of the wild-type PrP(107-143) after 10 ns of MD simulation (WT, Run 6).

C. Final shots of PrP(107-143;G127V) in four consecutive runs (G127V, Run 1-4) of 10 ns of MD simulations, and a graph showing proximity scores for residues in the U-shaped loop. The bars and error bars represent mean ± standard deviation (SD) of values from ten independent runs of simulation. Asterisks indicate $p < 0.05$.

D. A final shot of PrP(107-143;M129V) after 10 ns of MD simulation (M129V, Run 7).

E. Heat maps showing Avg-β and the SD-β of each residue of the wild type (WT) and the mutant PrP(107-143) amyloids (M129V and G127V). The values were calculated from ten independent runs of 10 ns. Blue boxes, more demarcated loop(116-119) than in WT. Red boxes, more stable β-sheet(128-133) with lower SD-β values. Black boxes, disordered loop(123-127).

F. Graphs comparing proximity scores between two residues around the U-shaped loop (upper left), the C-terminal region (lower left) and more N-terminal-side region (lower right).

Figure 5

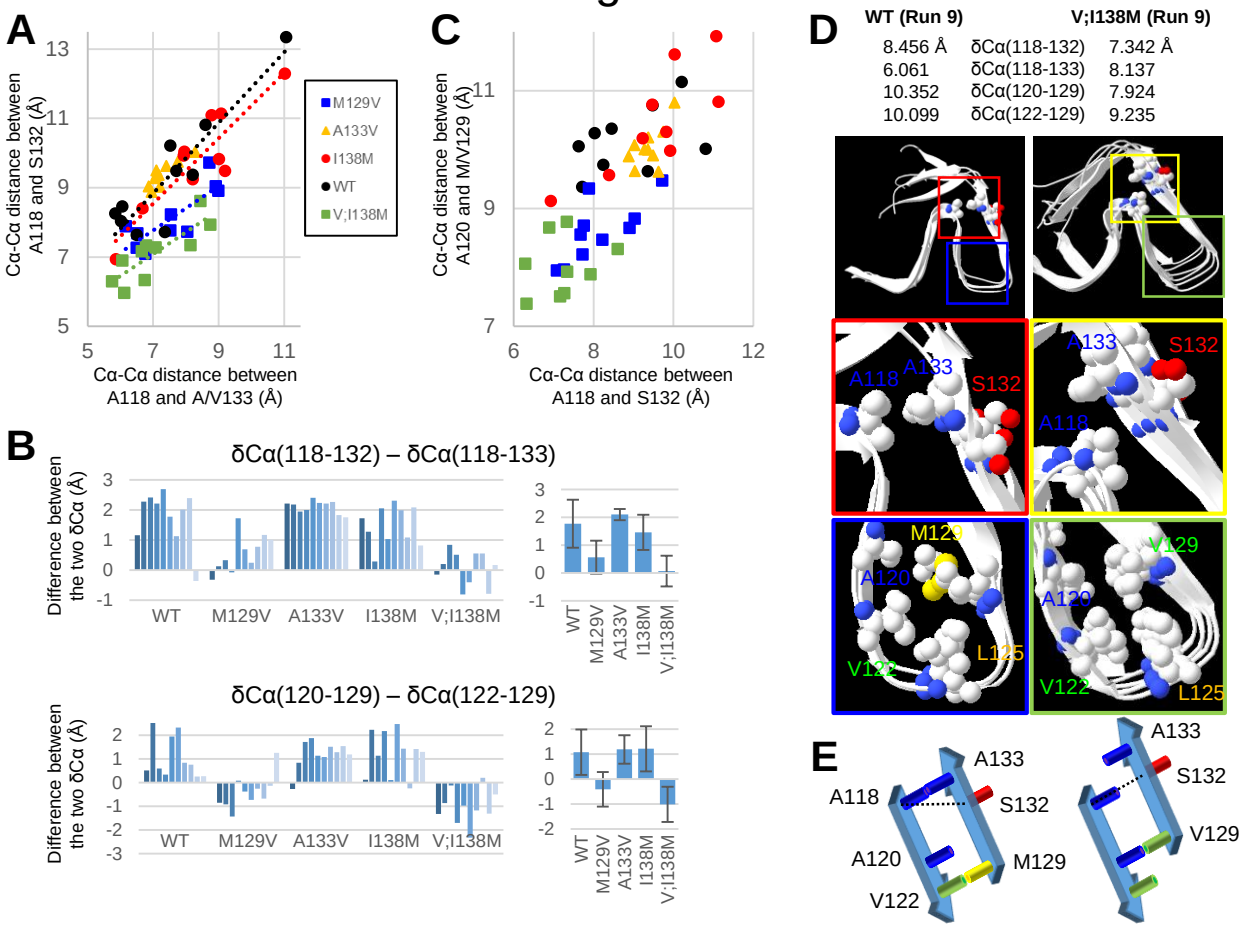

Fig 5. M129V mutation alters positional relations of β-sheet(120-122) and β-sheet(128-133).
A. A scatter plot showing correlations of the final Cα-Cα distances between A118-S132 (δCα(118-132)) and A118-A133 (δCα(118-133)) in the wild type and various mutant PrP(107-143) amyloids. WT, wild-type PrP(107-143). M129V, PrP(107-143;M129V). A133V, PrP(107-143;A133V). I138M, PrP(107-143;I138M). V;I138M, PrP(107-143;M129V;I138M).
B. Graphs showing differences between final δCα(118-132) and δCα(118-133) (upper graphs) and between final δCα(120-129) and δCα(122-129) (lower graphs) in the wild type and various mutant amyloids. The bars in the left graphs that get gradually paler represents the respective values of Run 1 to 10 of each amyloid. The right-hand side graphs show mean ± SD of the ten runs.
C. A scatter plot showing correlations of δCα(118-132) and δCα(120-129) in the wild type and various mutant PrP(107-143) amyloids. Note that δCα(120-129) of those with V129M mutation (blue and green squares) are shorter than 9 Å in most of the runs, and their δCα(118-132) values also tend to be shorter than those of the other mutants.
D. Final shots of chains D-G of PrP(107-143) and chains C-H of PrP(107-143;M129V) after 10 ns of MD simulation (WT and M129V, respectively). The insets show magnified views with side chains of residues involved in hydrophobic interactions.
E. A schematic illustration of the positional relations and "upward shift" of β-sheet(128-133) by M129V mutation. The dashed lines indicate distances between Cα carbons of A118 and S132.

Figure 6

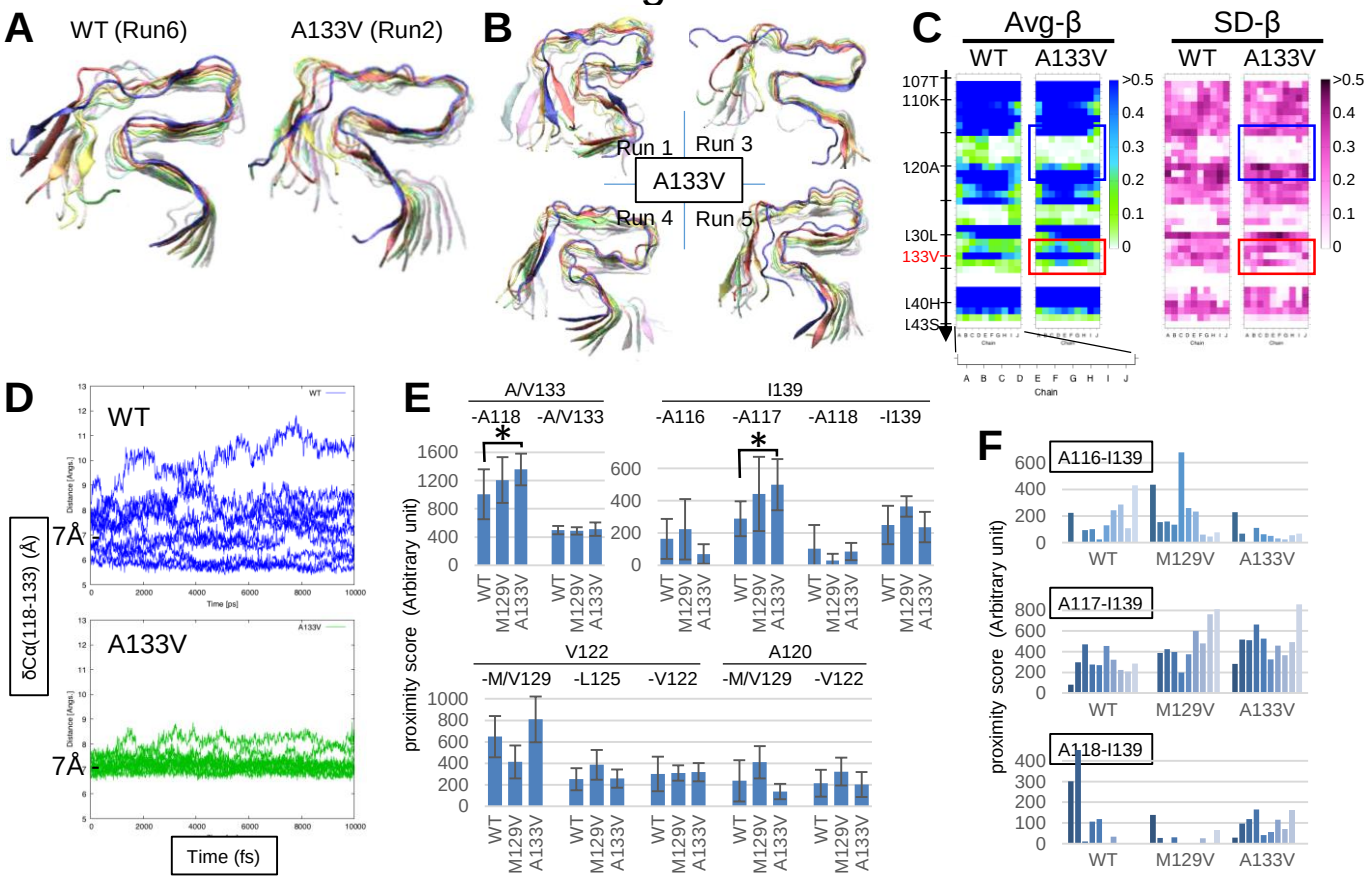

Fig 6. Influences of A133V mutation on the structures of the amyloid.

A. A representative final shot of PrP(107-143;A133V), A133V, after 10 ns of MD simulation, showing the U-shaped loop from the side (right panel), compared with that of the wild type (WT; left panel).

B. Final shots of the A113V mutant in run 1, 3, 4 and 5. The rest of the ten runs are presented in **Supplementary Fig S3**.

C. Heat maps comparing Avg-β and SD-β values between WT and A133V amyloids calculated from ten independent runs of 10 ns. Blue boxes, more demarcated loop(116-119). Red boxes indicate more stable β-sheet propensity at V133 with lower SD values than in WT.

D. Graphs showing fluctuations of average distances between Cα of A118 and A/V133, δCα(118-133), over 10 ns. Each line represent the average of the distances of chain A-J in each of ten runs.

E. Graphs of proximity scores of different regions comparing between WT and the mutants. The bars and error bars represent mean ± SD of values from ten independent runs of simulation. Asterisks indicate $p < 0.05$. Note that the scores for V122-M129 interactions tend to be higher and reciprocally lower for A120-M129 in the A133V mutant than in WT, although the differences were not statistically significant.

F. Graphs of proximity scores for A116-I139 (top), A117-I139 (middle) and A118-I139 (bottom). Bars that get gradually paler represents the respective values of Run 1 to 10 of each mutant.

Figure 7

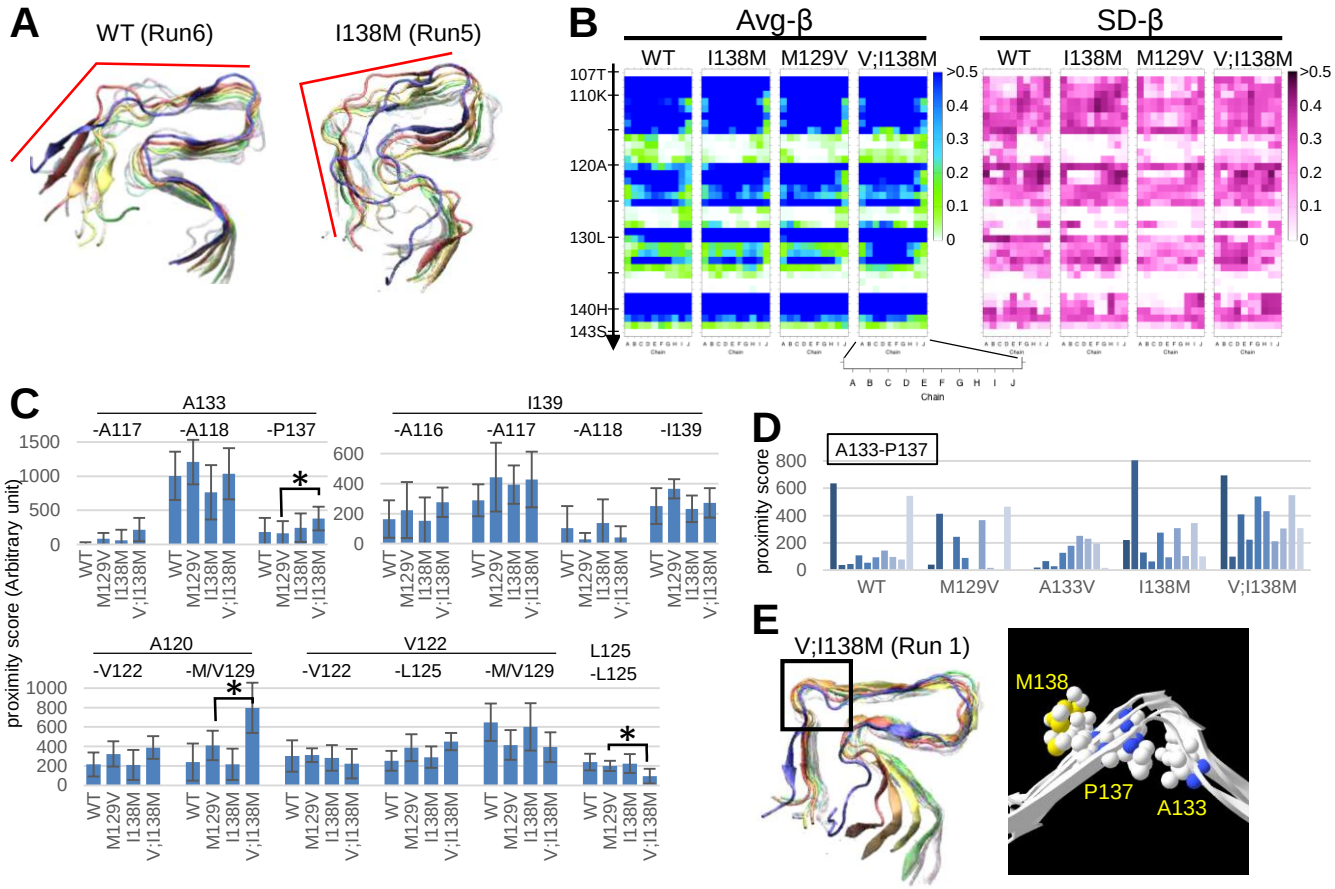

Fig 7. I138M mutation bends loop(134-137) deeper, and the effect is accentuated by V129M mutation.

A. A final shot of PrP(107-143;I138M), I138M, after 10 ns of MD simulation (right panel), compared with that of the wild type (WT; left panel). Note that the angles between β-sheet(128-133) and β-sheet(138-141) are near-square in I138M, whereas WT has obtuse angles. The rest of the ten runs are presented in **Supplementary Fig S3**.

B. Heat maps comparing Avg-β and SD-β values between WT, I138M, M129V and PrP(107-143;M129V;I138M), V;I138M. The values were calculated from results of ten independent runs of 10-ns simulations.

C. Graphs of proximity scores of different regions comparing WT and the mutants. The bars and error bars represent mean ± SD of values from ten independent runs of simulation. Asterisks indicate $p < 0.05$. Note that significant differences are mainly seen between mutants with M129V mutation, i.e., M129V and V;I138M, whereas WT and I138M show rather similar values.

D. Graphs of proximity scores for A133-P137. Each bar represents the value from each of the ten runs, Run 1 to 10.

E. A final shot of PrP(107-143;V129M;I138M), Run 1 (left panel). The box indicates Ω-shaped loops encompassing A133 to P137. Positional relations of side chains of A133, P137 and M138 in chain B-F (right panel).

Supplementary Figure S1

A The time course of MD simulation of 400 ns.

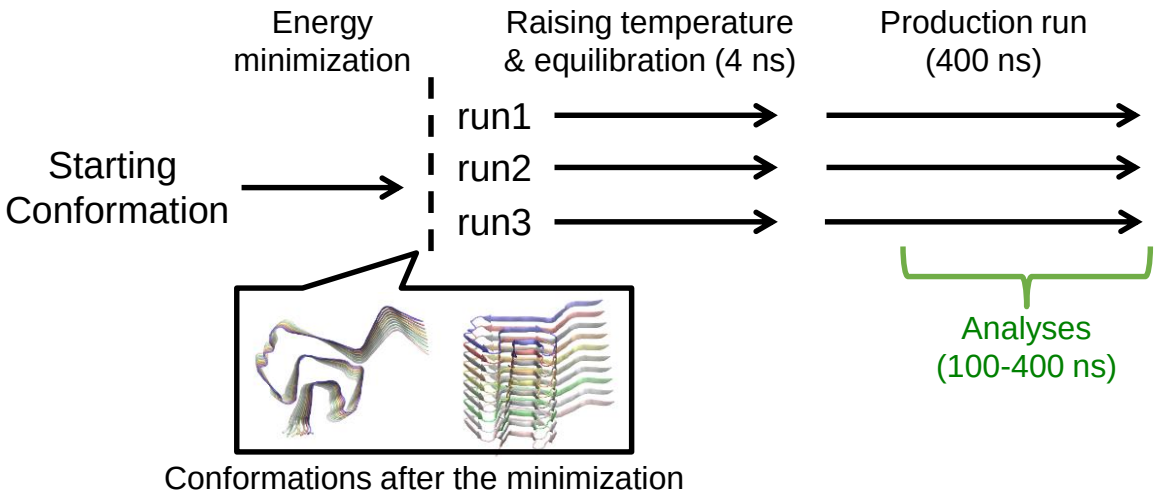

B The time course of short MD simulation of 5 ns of αSyn mutant amyloids re-modeled based on the "energy-minimized" αSyn(G84M) mutant amyloid.

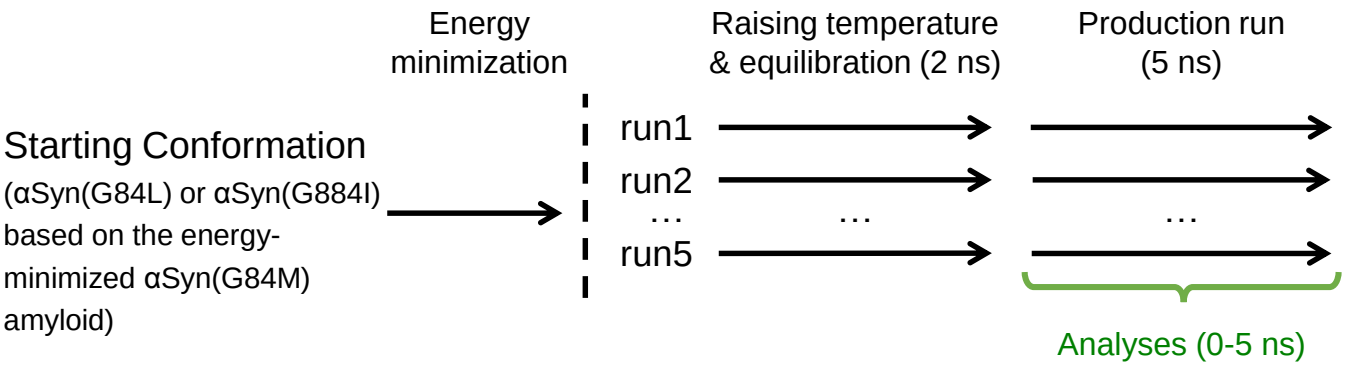

C The time course of MD simulation (10 ns) of the tentative local structural model of PrP^{Sc}, PrP(107-143) amyloids

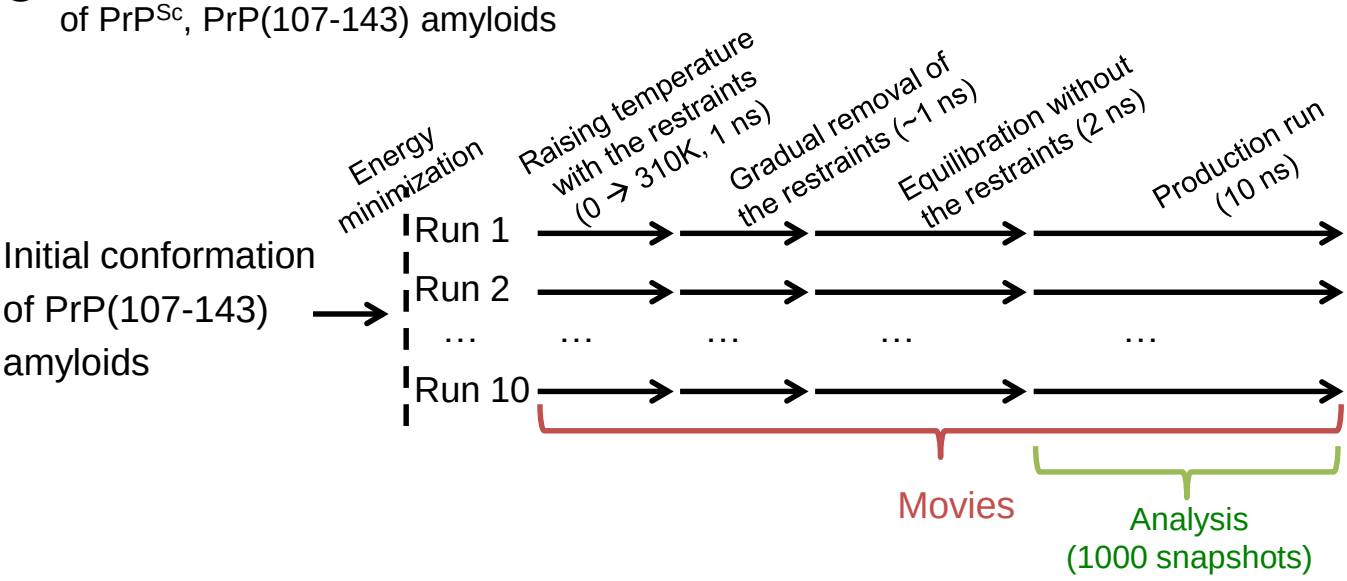

Supplementary Fig S2

A. Definition of Hydrophobic Contact & proximity score. A "hydrophobic contact" is counted when the distance between the centers of mass (red dots ● in Fig S2A) of two hydrophobic residues are within 5 Å [60]. For example, in **Fig S2A**, V122-M129 and A120-V122 are counted as contacts but M129-A120 is not. "proximity score" basically sums up the proportions of time/snapshots in a 10-ns run when hydrophobic contact is present between the two residues of interest over chains A-J. When a single residue has hydrophobic contact simultaneously with the residue on the same chain and another residue of the same residue number on the next chain, the score for the interaction in the snap shot is two. Therefore, the total proximity score can be larger than 1000 if there are many inter-chain interactions.

B. Correlations between Cα-Cα distances between two residues of interest and the corresponding proximity scores.

C. Diagrams of proximity scores of the wild type and the mutant PrP(107-143) amyloids with the nodes positioned in the similar spatial relations in the amyloids. Values of proximity scores are represented by both thickness and colors of the bonds. Looped bonds represent interactions between the residues of the same residue number on different chains.

A

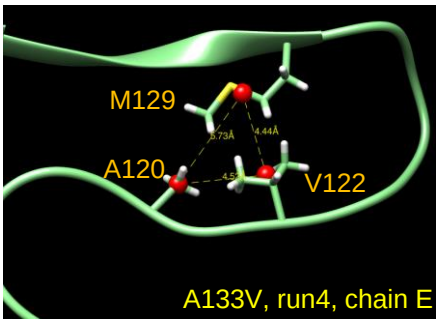

Distances between the centers of mass

A120-M129	5.73 Å
V122-M129	4.44 Å
A120-V122	4.52 Å

B

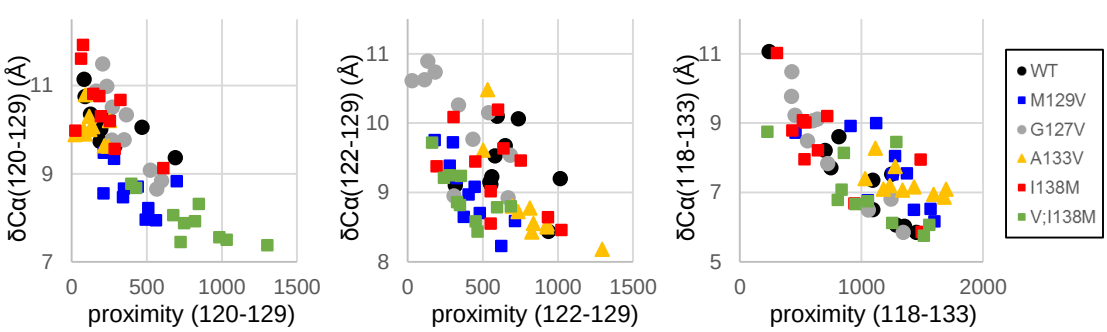

C

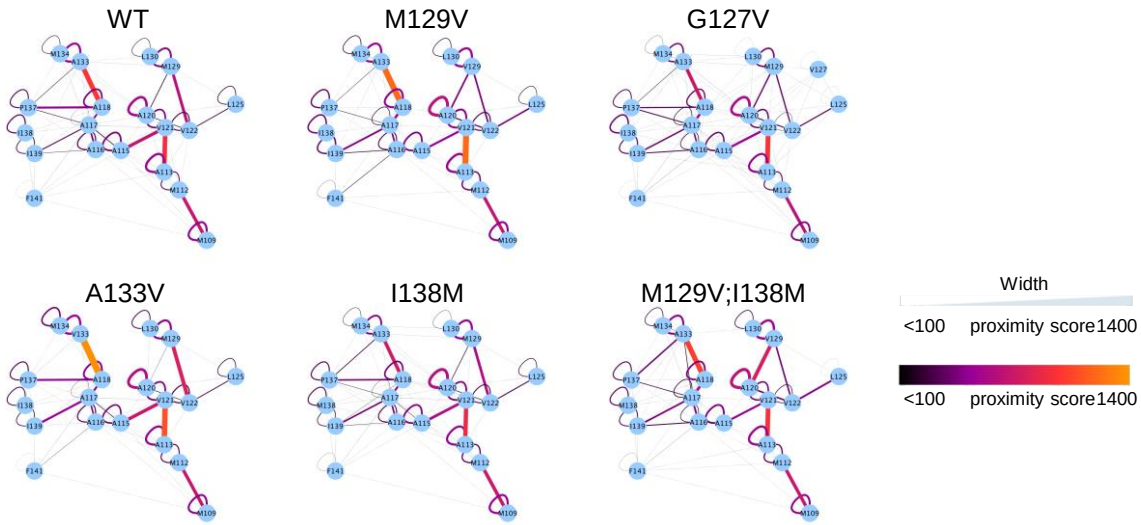

Supplementary Fig S3

Final shots of the ten independent runs of simulation are presented. Those with proximity scores for A133-P137 higher than 200 are in black boxes. As for “M129V;I138M”, most of them showed the proximity scores >200, except for two: “Run 2” (red box) had the proximity score lower than 200 (specifically, 99.4) and that of “Run 7” (yellow box) was barely higher (211.3).

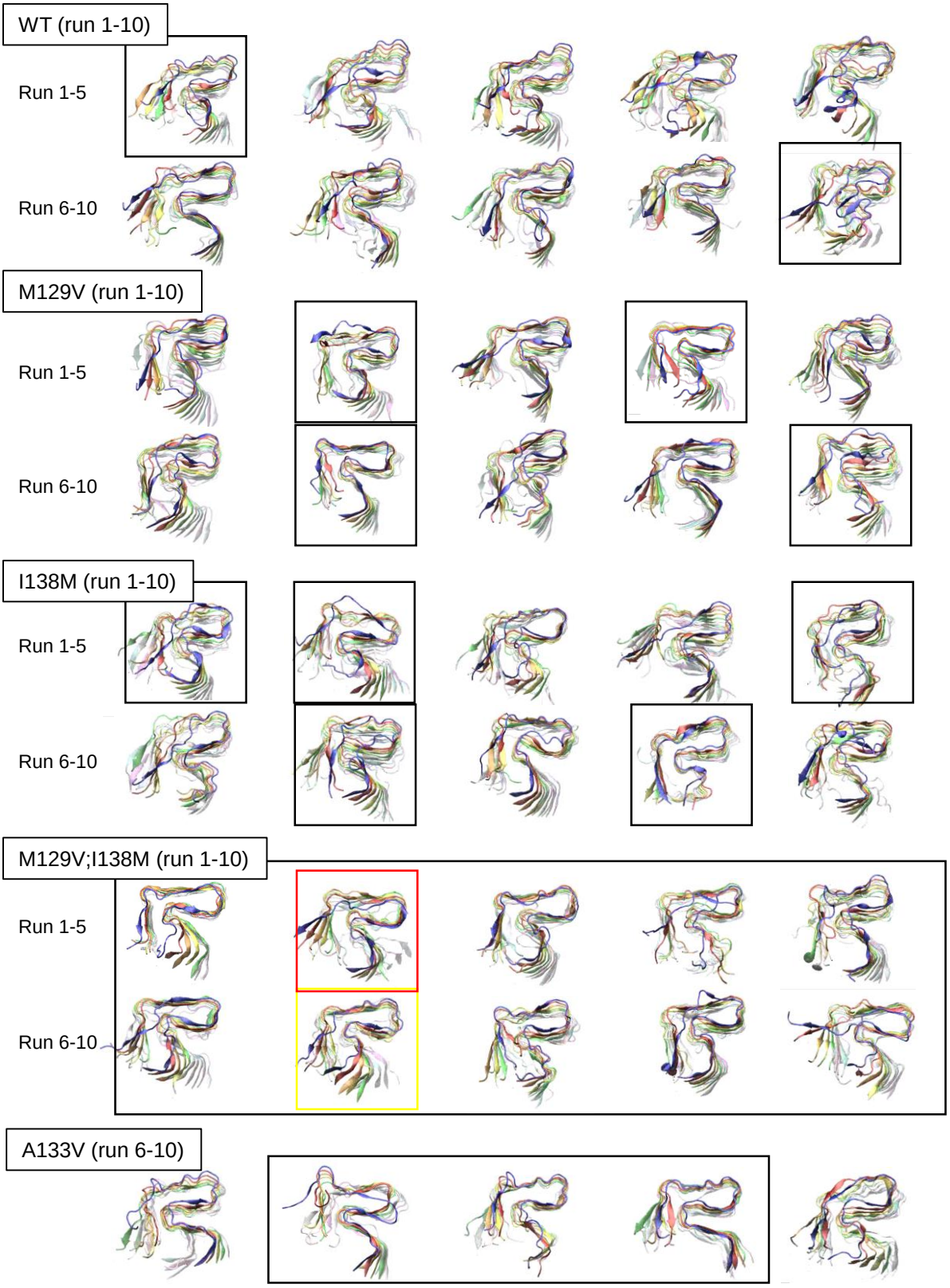

Supplementary Fig S4
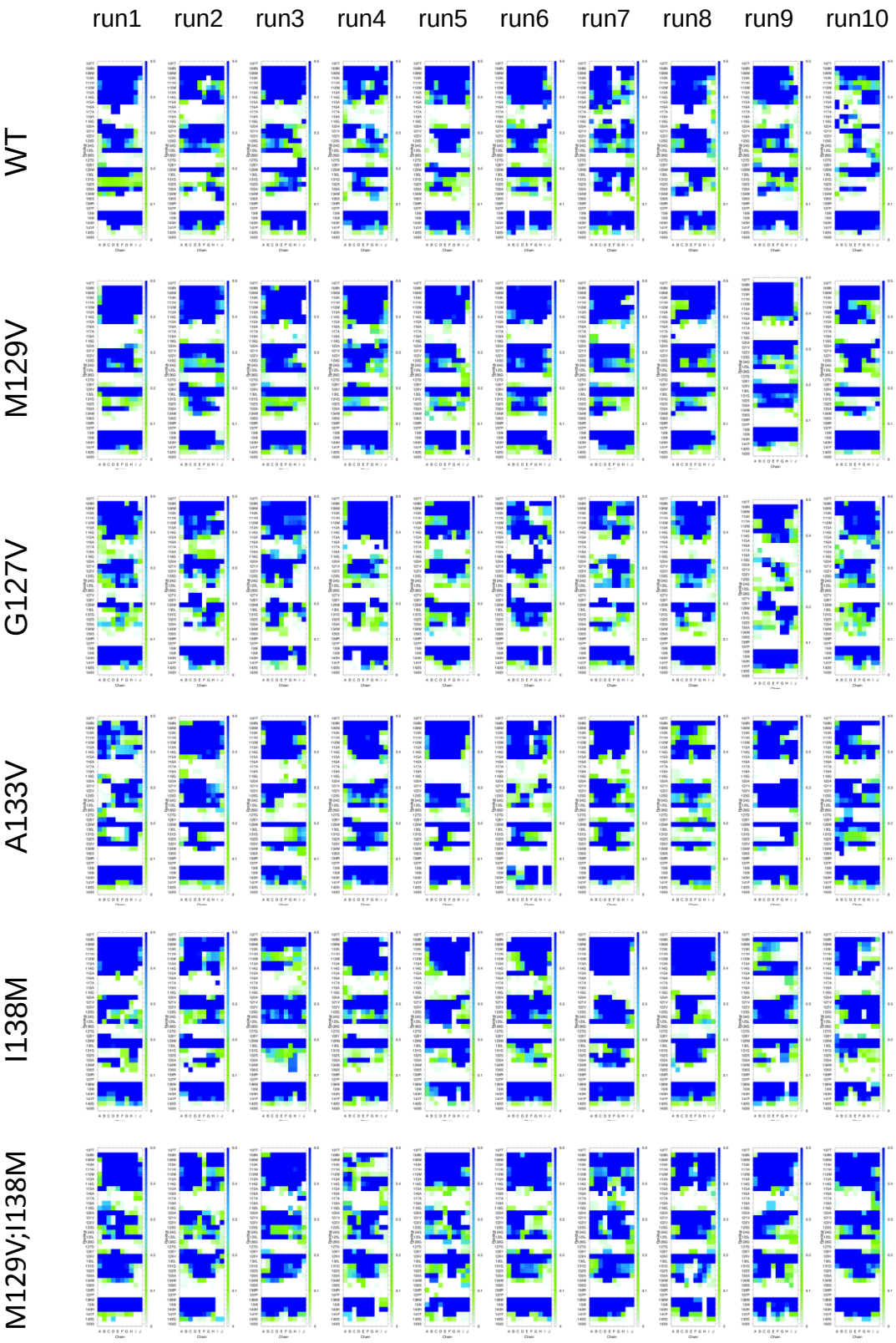
Heat maps of Avg-β of all the runs